

Inhibition of the IL-17A axis Protects against Immune-related Adverse Events while Supporting Checkpoint Inhibitor Anti-tumor Efficacy

Melissa Lechner (✉ mlechner@mednet.ucla.edu)

UCLA Geffen School of Medicine <https://orcid.org/0000-0002-4744-6566>

Anushi Patel

UCLA Geffen School of Medicine

Willy Hugo

UCLA

Trevor Angell

USC Keck School of Medicine

Ho-Chung Chen

UCLA Geffen School of Medicine

Marissa Pioso

UCLA Geffen School of Medicine

Aline Hoang

UCLA Geffen School of Medicine

Natalie Yakobian

UCLA Geffen School of Medicine

Ethan McCarthy

UCLA Geffen School of Medicine

Eduardo Rodriguez

UCLA Geffen School of Medicine

Mandy Cheng

UCLA Geffen School of Medicine

Lily Guo

UCLA Geffen School of Medicine

Alexandra Drakaki

UCLA Geffen School of Medicine

Antoni Ribas

University of California, Los Angeles <https://orcid.org/0000-0003-3669-8458>

Marueen Su

University of North Carolina

Article

Keywords: Checkpoint Inhibitor Immunotherapy, Immune Related Adverse Events, Thyroiditis, Type 3 Immune Cells

Posted Date: June 30th, 2021

DOI: <https://doi.org/10.21203/rs.3.rs-609476/v1>

License:   This work is licensed under a Creative Commons Attribution 4.0 International License.
[Read Full License](#)

1 Inhibition of the IL-17A axis Protects against Immune-related Adverse Events while
2 Supporting Checkpoint Inhibitor Anti-tumor Efficacy

3
4
5 Melissa G. Lechner, MD, PhD^{1*}, Anushi Y. Patel², Willy Hugo, PhD³, Trevor E. Angell, MD⁴, Ho-
6 Chung Chen, BS², Marissa S. Pioso, BS², Aline T. Hoang, BS², Natalie Yakobian, BS², Ethan C.
7 McCarthy², Eduardo D. Rodriguez, MD⁵, Mandy I. Cheng, BA², Lily Guo, BS², Alexandra
8 Drakaki, MD, PhD⁶, Antoni Ribas, MD, PhD⁶, and Maureen A. Su, MD^{2,7}

9
10 **Affiliations:**

- 11 1. Division of Endocrinology, Diabetes, and Metabolism, UCLA David Geffen School of
12 Medicine, Los Angeles, CA
- 13 2. Department of Microbiology, Immunology, and Molecular Genetics, UCLA David Geffen
14 School of Medicine, Los Angeles, CA
- 15 3. Division of Endocrinology and Diabetes, USC Keck School of Medicine, Los Angeles,
16 CA
- 17 4. Division of Dermatology, Department of Medicine, UCLA David Geffen School of
18 Medicine, Los Angeles, CA
- 19 5. Department of Pathology, UCLA David Geffen School of Medicine, Los Angeles, CA
- 20 6. Division of Hematology and Oncology, UCLA David Geffen School of Medicine, Los
21 Angeles, CA
- 22 7. Division of Pediatric Endocrinology, UCLA David Geffen School of Medicine, Los
23 Angeles, CA
- 24

25 **ABSTRACT**

26 **Checkpoint inhibitor (ICI) immunotherapy leverages the body's own immune system to**
27 **attack cancer cells but leads to unwanted autoimmune side effects in up to 60% of patients.**
28 **Such immune related adverse events (IrAE) lead to treatment interruption, permanent**
29 **organ dysfunction, hospitalization and premature death. Thyroiditis is one of the most**
30 **common IrAE, but the cause of thyroid IrAE remains unknown. Here we present a novel**
31 **mouse model in which checkpoint inhibitor therapy leads to multi-organ autoimmune**
32 **infiltrates and show that activation and infiltration of Type 3 immune cells including IL17A⁺**
33 **ROR γ t⁺ CD4⁺ (T helper 17 or Th17) and gamma delta 17 ($\gamma\delta$ T17) T cells promote thyroid IrAE**
34 **development. In parallel, Th17 and $\gamma\delta$ T17 cells were similarly expanded in cancer patients**
35 **treated with ICI. Furthermore, antibody-based inhibition of IL-17A, a clinically available**
36 **therapy, significantly reduced thyroid IrAE development in ICI-treated mice. Finally,**
37 **combination of IL-17A neutralization with ICI treatment in a mouse tumor model did not**
38 **reduce ICI anti-tumor efficacy and indeed showed a trend toward enhancement. These**
39 **studies suggest that targeting Th17 and $\gamma\delta$ 17 function may reduce IrAE without impairing**
40 **ICI anti-tumor efficacy and may be a generalizable strategy to address IL17-mediated IrAE.**

41 INTRODUCTION

42 Immune checkpoint inhibitors (ICI) against programmed death protein (PD-1) and cytotoxic T
43 lymphocyte antigen (CTLA)-4 have revolutionized cancer therapy and hold great promise for the
44 treatment of advanced malignancies¹. Since initial approval in 2011, seven ICI have entered
45 clinical care, with nearly half of patients with cancer in the U.S. eligible for ICI treatment². ICI are
46 used for first line therapy of metastatic renal, bladder, head and neck, liver, and certain lung,
47 colon, and breast cancers². However, the benefits and use of ICI are limited by development of
48 autoimmune side effects, termed immune related adverse events (IrAEs) seen in up to 60% of
49 patients³⁻⁵. Endocrine, gastrointestinal and liver, and dermatologic tissues are some of the most
50 common affected by IrAEs^{3,4,6}. Pulmonary, neurologic, renal, and cardiac autoimmune side effects
51 from ICI are less frequent but associated with grave clinical consequences, including mortality
52 rates of 17-40%⁷. IrAEs can lead to permanent organ dysfunction, cancer therapy interruption,
53 hospitalization, and premature death^{5,7}. With the expanding use of ICIs, IrAEs represent a growing
54 clinical problem.

55
56 Despite significant efforts to date, the mechanisms of IrAE remain poorly understood⁸. Thyroiditis
57 is one of the most common ICI-associated IrAE, occurring in approximately 10-15% of patients
58 treated with anti-PD1/L1 monotherapy and 30% of patients treated with combination anti-PD-1/L1
59 and CTLA-4^{6,9,10}. Like IrAE in other organs, ICI-thyroiditis has both overlapping and distinct
60 features with spontaneous autoimmunity (*i.e.* Hashimoto's thyroiditis, HT)⁹⁻¹². Two prior important
61 studies^{13,14} showed lymphocyte accumulation in ICI-thyroiditis, similar to HT. The onset of
62 thyroiditis during ICI-treatment may be due to the release of immune checkpoints on pre-existing,
63 thyroid-reactive T cells, as suggested by the progressive loss of gland function in patients with
64 HT and increased risk of ICI-thyroiditis in patients with baseline thyroid autoantibodies to thyroid
65 peroxidase (TPO)^{13,15,16}. On the other hand, thyroid gland destruction in ICI-thyroiditis is much
66 more rapid compared to spontaneous HT and usually with a clear hyperthyroid phase during gland

67 destruction and subsequent evolution to permanent hypothyroidism^{9,12}. Many patients with ICI-
68 thyroiditis also lack the usual anti-thyroid antibodies to TPO or thyroglobulin (Tg) seen in HT at
69 diagnosis^{9,12}. Thus ICI-thyroiditis, while similar to HT, may be driven by the additional presence
70 of novel immune mechanisms and antigens.

71
72 To develop ICI therapies with less toxicity while preserving anti-tumor efficacy, we must determine
73 the cause of IrAE. Currently guidelines recommend suspension immunotherapy and high dose
74 glucocorticoid therapy for severe manifestations (grade 3 or 4) of most IrAE^{17,18}, which may
75 unnecessarily impair the efficacy of ICI cancer treatment for many patients^{5,19}. It is now recognized
76 that high dose glucocorticoid therapy does not attenuate or prevent thyroiditis, hypophysitis, or
77 diabetes, and correlates with shorter overall survival^{12,20,21}. Recent data in gut ICI-induced IrAE
78 suggested that immune adverse events may be uncoupled from anti-cancer efficacy using anti-
79 inflammatory treatments²². Studies of ICI-associated IrAE in the thyroid may identify common
80 mechanisms driving IrAE development in organs with more grave clinical consequences (*e.g.*
81 pneumonitis). In this study, we define immune mechanisms underlying thyroid IrAE from
82 checkpoint immunotherapy using a newly developed mouse model and translational studies in
83 patients with ICI-thyroiditis. High dimensional analysis of peripheral and thyroid-infiltrating
84 immune cells revealed recruitment and activation of type 3 immune cells including IL17A⁺ ROR γ t⁺
85 CD4⁺ (T helper 17 or Th17) and gamma delta 17 ($\gamma\delta$ T17) T cells. Moreover, pre-clinical studies
86 demonstrate that IL-17 blockade effectively protects against ICI-thyroiditis without negatively
87 impacting ICI-mediated anti-tumor immunity.

88

89 **RESULTS**

90 *The NOD background strain predisposes mice to ICI-IRAEs that mimic those seen in humans*

91 The study of ICI-associated IrAE has been hindered by the lack of robust preclinical models⁸.
92 While prior studies have reported autoimmunity in ICI-treated mice, these models on the C57BL/6
93 (B6) background developed minimal ICI-IrAEs. Augmenting these mild phenotypes required
94 significant manipulation, such as regulatory T cell depletion²³, genetic knock-in of human
95 checkpoint proteins²⁴, chemical stimulants²⁵ or co-administration of complete Freund's adjuvant¹⁹.
96 A recent paper utilized CBA/J mice in a thyroid IrAE model, but IrAE induction required non-
97 physiologic immunization with human thyroglobulin²⁶. We sought to develop a murine model of
98 ICI-IrAE that better recapitulated the development of IrAE in patients; namely, treatment-
99 dependent incident multi-system autoimmune infiltration in an immune competent host. We first
100 sought to establish a baseline for ICI-IrAE in the wild type B6 strain. Groups of four- to six-week
101 old B6 mice were treated twice weekly with anti-mouse CTLA-4 (clone 9D9) and PD-1 (RPM1-
102 14) antibodies or isotype controls (2A3, MPC-11), at 10 mg/kg/dose *i.p.*, as outlined in **Fig. 1a**. We
103 chose to treat with dual ICI therapy (combination anti-CTLA-4/PD-1) since the combination has
104 been linked with the highest rates of ICI-IrAEs^{3,4}. Mice were monitored at least twice weekly for
105 signs of autoimmunity, including weight loss, decreased activity, and glucosuria. After 4 weeks of
106 treatment, mice were sacrificed, and multiple tissues (salivary, lacrimal, pancreas, liver, lung,
107 heart, colon, eye, gonad, and thyroid) were evaluated by histology and flow cytometry for the
108 development of autoimmune infiltrates. Tissue immune infiltration was quantified by blinded
109 assessment of hematoxylin and eosin (H&E)-stained formalin fixed paraffin-embedded (FFPE)
110 sections (5 high powered fields/section in each animal). Sera were collected for measurement of
111 thyroid autoantibodies to Tg and TPO, as previously described²⁷. Overall mice were resistant to
112 ICI-induced autoimmunity with immune infiltration limited on average to two organs per mouse
113 (**Fig. 1b**). Increased immune infiltrates were seen in the liver and lacrimal glands, but not in the
114 thyroid (**Fig. 1b** and **Extended Data Fig. 1**). Additionally, B6 mice did not develop thyroid
115 autoantibodies to thyroid peroxidase (TPO) or thyroglobulin (Tg) (**Fig. 1c**). Furthermore, weights
116 remained stable in ICI and isotype treated mice, and survival was unchanged by ICI treatment

117 during the experimental period (data not shown). Similar results were seen in mice treated with
118 ICI or isotype for eight weeks (data not shown). In summary, B6 mice failed to develop significant
119 multisystem autoimmunity with combination anti-PD1 and anti-CTLA-4 immune checkpoint
120 inhibitor (Dual ICI) therapy. These findings are in keeping with previous reports that B6 mice are
121 resistant to spontaneous autoimmunity, perhaps due to genetic polymorphisms that alter immune
122 responses in this inbred strain^{28,29}.

123

124 Underlying subclinical autoimmunity or genetic predisposition increases risk of developing IrAE
125 during ICI cancer therapy in patients^{15,20,30}. For example, patients with thyroid auto-antibodies
126 against thyroid peroxidase at baseline were five-fold more likely to develop thyroiditis with ICI
127 treatment^{11,31}. The NOD mouse is an autoimmune-prone inbred strain that is best known for its
128 contributions to type 1 diabetes studies but has also been invaluable in understanding generalized
129 autoimmunity³². NOD mice develop spontaneous autoimmunity in multiple tissues including
130 thyroiditis, at low frequency (14% at 52 weeks)^{33,34}. Thus, we tested whether IrAE development
131 may be more robust and reproducible in NOD mice compared to B6. As done in B6 mice, four- to
132 six-week old NOD mice were treated twice weekly with anti-mouse CTLA-4, PD-1, both (Dual ICI),
133 or isotype control and then autoimmune tissue infiltrates and thyroid autoantibodies evaluated.

134

135 ICI-treated NOD mice developed increased immune infiltrates in multiple tissues (*e.g.* thyroid,
136 colon, liver, lung, salivary and lacrimal glands) compared to isotype-treated animals, as shown in
137 **Fig. 1d-e** and **Extended Data Fig. 2** (ANOVA $p < 0.0001$; p values vs. isotype were < 0.0001 for
138 anti-CTLA-4, anti-PD-1, and Dual ICI). The predominant inflammation in the thyroid consisted of
139 lymphocytic aggregates within the interstitium and occasionally perivascular aggregates. In the
140 liver, both focal collections of lymphocytes within liver parenchyma and peri-portal venule sites
141 were seen. Lung tissues similarly showed aggregates of focal lymphocyte aggregation, as well
142 as loss of alveolar air spaces. Histologic examination of the colon sections showed areas with

143 neutrophilic cryptitis, crypt epithelial apoptosis, and rare neutrophilic microabscesses. Increased
144 intraepithelial lymphocytes were not detected, but basal lymphoplasmacytosis was focally seen.
145 The pattern of immune infiltration in the kidney was primarily glomerulonephritis with accumulation
146 of lymphocytes, and occasionally peri-vascular lymphocytic aggregates. In the pancreas, immune
147 infiltration was centered on islet and peri-vascular areas, with lymphocytic infiltration of 25-100%
148 of islets in most ICI-treated animals. Finally, salivary and lacrimal glands showed interstitial
149 lymphocyte aggregates often with diffuse gland involvement. One animal developed pericardial
150 inflammation. Eye, adrenal, myocardial, and gonad tissues were also evaluated, and autoimmune
151 infiltrates were not seen in any animals. As in patients, autoimmunity occurred more frequently
152 with the combination of anti-PD-1 + anti-CTLA-4 vs. with single agent ICI. In addition, mice
153 developed thyroid autoantibodies to TPO and Tg (**Fig. 1f**) and, as expected, showed acceleration
154 of underlying autoimmune risk (*i.e.* diabetes, data not shown)^{11,20}. Mice developing diabetes were
155 treated with insulin, as described previously³⁵. Thyroid hormone status was evaluated at 8 weeks
156 by serum measurement of free thyroxine. ICI-treated mice had increased mean thyroxine serum
157 concentrations compared to isotype controls, consistent with excess thyroid hormone release and
158 hyperthyroxinemia during the early destructive phase of ICI-thyroiditis (**Fig. 1g**). Furthermore,
159 some ICI-treated mice notably exhibited low serum thyroxine consistent with the conversion to
160 hypothyroidism over time in ICI-thyroiditis and mirroring the earlier conversion to hypothyroidism
161 in Dual vs. single agent therapy seen in patients.⁹

162

163 During the 8-week treatment period, the rate of spontaneous autoimmunity was low in isotype-
164 treated controls which developed only pancreatic insulinitis and occasional lacrimal or salivary
165 gland focal immune infiltration at 12-15 weeks of age (**Fig. 1d-e**), consistent with their NOD
166 background. Thus, our mouse model recapitulates critical features of clinical ICI-associated
167 autoimmunity and thus will facilitate studies of the mechanisms leading to IrAEs.

168

169 **Multiple IL-17A-producing cell types are increased in the periphery of ICI-treated mice**

170 To define immune changes occurring with ICI-associated autoimmunity, we measured the
171 frequency and activation status of different immune populations in ICI- vs. isotype-treated mice.
172 In the ICI-treated animals, we noted increased frequency of pan-CD3⁺ T cells among splenocytes
173 (mean 49±2 SEM 2 vs 41±1.6, adjusted p=0.047, **Fig. 2a**), and effector/memory (CD44⁺CD62L⁻)
174 subsets among CD4⁺ and CD8⁺ T cells, compared to isotype antibody-treated control mice (**Fig.**
175 **2b**; adjusted p<0.001 for both). No difference (or a slight decrease) was seen in the frequency of
176 B cells (B220⁺, mean 41±1.8 vs 46.6±1.6, p=ns), dendritic cells (CD11c⁺CD11b^{low}, mean 1.4±0.1
177 vs 1.7±0.1, p=ns) and myeloid cells (CD11b⁺CD11c⁻B220⁻, mean 2.5±0.2 vs 2.8±0.2, p=ns), NK
178 (NKp46⁺CD3⁻, mean 1.5±0.1 vs 2.8±0.2, p<0.0001) and NKT cells (NKp46⁺CD3⁺, mean 0.3±0.02
179 vs. 0.5±0.01, p<0.0001) (**Extended Data Fig. 3**). T cell expansion and activation following anti-
180 PD-1 and/or anti-CTLA-4 treatment has been reported previously^{36,37}. We then evaluated cytokine
181 production by T cells in Dual ICI-treated mice to understand how their activation may skew overall
182 immune responses and potentially lead to the observed autoimmunity. We saw no significant
183 difference in interferon (IFN)- γ producing CD4⁺ T cells from ICI-treated vs. isotype mice (2.1±0.3
184 vs. 2.6±0.4 percent of CD4⁺ T cells, p=ns, **Fig. 2c**). IL-17A⁺ CD4⁺ helper T cells (Th17), on the
185 other hand, were significantly increased in ICI-treated mice compared to isotype controls (2.1±0.1
186 vs. 1.4±0.2 percent of CD4⁺ T cells, p<0.001, **Fig. 2d**). Consistent with this finding, CD4⁺ T cells
187 in ICI-treated mice also had increased expression of Th17-associated transcription factor ROR γ t
188 (**Fig. 2e**). IL-17A-expressing CD4⁺ Th17 cells have been previously implicated in the
189 pathogenesis of multiple spontaneous autoimmune diseases, including Hashimoto's thyroiditis,
190 but have yet to be reported in IrAE³⁸⁻⁴¹. Surprisingly, IL-17A⁺ immune cells lacking CD4
191 expression (CD4⁻) were also significantly increased in ICI-treated mice (**Fig. 2f**, p=0.005). IL-17A
192 can be produced not only by Th17 but also by other immune cells including IL-17-producing
193 gamma delta cells ($\gamma\delta$ T17) and Group 3 innate lymphoid cells (ILC3s)⁴²⁻⁴⁴. Thus it is possible that

194 these CD4⁻ IL-17A⁺ cells represent gamma delta T cells or innate lymphoid cells. As shown in
195 **Fig. 2g**, IL-17A⁺ $\gamma\delta$ T cells were indeed increased in ICI-treated compared to isotype mice
196 ($p=0.03$). From these data, we hypothesized that IL-17A-producing cells from multiple lineages,
197 including Th17 and $\gamma\delta$ T17, contribute to ICI-immune-related toxicities in our mouse model.

198

199 ***Diverse infiltrating immune cells in the thyroid of ICI-treated mice***

200 Given that ICI treatment increases thyroid immune infiltration in NOD mice (**Fig. 1**), we used a
201 multi-modal strategy to delineate the cellular composition within the thyroid infiltrate.
202 Immunohistochemical staining for canonical immune markers on FFPE sections showed the
203 presence of T cells (CD3), macrophages (F4/80), and B cells (B220) in immune aggregates in
204 ICI-treated mice, with rare immune cells in the thyroid parenchyma of isotype controls (**Fig. 3a**).
205 We then quantified immune cells in thyroid tissues using flow cytometry as shown in **Fig. 3b-c**.
206 Fresh thyroid tissues from ICI or isotype-treated mice were perfused with saline and dissociated
207 into single cell suspensions then stained for immune markers and analyzed for CD45⁺-gated
208 immune cells. More infiltrating CD45⁺ immune cells were seen in thyroid tissue of ICI-treated mice
209 compared to isotype controls (mean 15,875 cells/thyroid \pm SEM 7,515 vs. 1,195 \pm 687, trend,
210 $p=0.057$) (**Fig. 3b**). T cells (CD3⁺) constituted the major group of the infiltrating immune cells
211 (CD45⁺) in thyroid tissue and were significantly increased in ICI-treated mice (mean 3,332 \pm 1,220
212 cells/thyroid lobe vs. 420 \pm 176, $p=0.02$). Other populations seen in thyroid immune infiltrates were
213 also more numerous in ICI-treated mice, including DCs (CD11c⁺ CD3⁻ F4/80⁻ B220⁻ CD11b^{low},
214 mean 46 \pm 9 vs. 16 \pm 5, $p=0.008$; CD11c⁺ CD3⁻ F4/80⁻ B220⁻ CD11b⁺ mean 214 \pm 37 vs. 73 \pm 13,
215 $p=0.001$), macrophages (F4/80⁺, mean 234 \pm 43 vs. 140 \pm 25), B cells (B220⁺ CD3⁻ CD11b⁻, mean
216 212 \pm 77 vs. 32 \pm 13, $p=0.03$), and NK cells (NKp46⁺CD3⁻, mean 221 \pm 74 vs. 46 \pm 16, $p=0.03$) (**Fig.**
217 **3c**). This diversity of immune cell populations suggests the dynamic interplay of multiple immune
218 cell types in the autoimmune response.

219

220 With the goal of precisely understanding the cellular composition and cell type-specific
221 inflammatory networks associated with thyroid IrAEs at a single cell resolution, we turned to single
222 cell RNA sequencing (scRNAseq) of CD45⁺ thyroid-infiltrating immune cells from Dual ICI-treated
223 mice (**Fig. 3d**). This technique facilitates identification of rare cell populations and characterization
224 of limited tissue specimens, as in the case of murine thyroid tissue (approximately 1mm³ of thyroid
225 tissue per animal). Sorted, live CD45⁺ cells from Dual ICI-treated NOD mice thyroid specimens
226 (*n*=10 animals) were used to construct Chromium™ 10x single cell 5' gene expression libraries
227 for single cell sequencing. The reads were mapped to the mouse reference genome using the
228 CellRanger pipeline. The transcript counts of each cell were subsequently analyzed using the
229 Seurat R package⁴⁵. Briefly, the cells from each sample were initially QC-ed to remove artifacts
230 with low sequencing coverage and/or high mitochondrial reads. The cells passing the QC were
231 clustered in order identify different immune cell populations. Fourteen heterogeneous immune
232 cell populations were identified and visualized using the uniform manifold approximation and
233 projection (UMAP) (**Fig. 3d**; total *n*=4,095 cells). Putative cell cluster identities in **Fig. 3d** were
234 made based upon expression of canonical population markers and functional gene expression
235 (**Extended Data Fig. 4a-b and Extended Data Table 1**). Specifically, lymphoid cell clusters
236 consisted of CD4⁺ T cells (Cd4: *Cd3e*, *Cd4*), CD8⁺ T cells (Cd8: *Cd3*, *Cd8a*), and gamma delta
237 ($\gamma\delta$) T cells (*Cd3e*, *Trdc*). T cell clusters were further defined as naive CD4 (*Sell*, *Ccr7*, *Satb1*,
238 *Foxp1*, *Lef1*, *S1pr1*), regulatory T cells (Treg: *Cd3e*, *Cd4*, *Foxp3*, *Ctla4*, *Ikzf2*, *Tnfrsf18* (GITR),
239 *ICOS*), effector CD4 (*Cd4*, *Cd40lg*, *Sh3bgrl3*, *Cd52*, *Id2*, *Ly6a*, *Cxcr3*, *Tmem176a/b*; or *Cd4*,
240 *Itga4*, *Eef1a1*, *Cd40lg*, *Cxcr3*, *Fasl*, *Icos*, *Ctla4*, *Id2*, *Nrp1*; or *Cd4*, *Ctla4*, *Cd40lg*, *Fasl*, *Cxcr4*,
241 *Ifng*, *Tnfrsf4*, *Tbx21*, *ICOS*, *Tnfaip3*, *Nfkb1a*), and effector CD8 (*Cd8a*, *Cd8b1*, *Gzmk*, *Ccl5*, *Nkg7*,
242 *Ly6a*, *Gzma*, *Klrd1*, *Prf1*). Myeloid cell populations included macrophages (*Cd68*, *Cd14*, *Fcgr1*,
243 *Adgre1*, *C1qa*, *C1qb*, *C1qc*, *Csfr1*, *Cd74*) and (monocytic) dendritic cells (DC/APC: *Cd68*, *Cd74*,
244 *Cd14*, *Itgax*, *H2-Aa*). Other immune clusters were innate lymphoid cells (ILC: *Il7r*, *Il1rb*, *Il13*, *Arg1*),

245 natural killer T cells (NK/NKT: *Ncr1*, *Cd7*, *Klra5*, *Klrd1*, *Fcer1g*, *Gzma*), and B cells (B: *Cd79a*,
246 *Cd19*, *Ebf1*, *Cd74*). These data confirm and provide further characterization of the diverse thyroid-
247 infiltrating immune cell populations seen by IHC and flow cytometry techniques in ICI-treated NOD
248 mice.

249

250 **Infiltrated thyroids of ICI-treated mice accumulate multiple lineages of *Rorc*-expressing** 251 **immune cells**

252 Single-cell RNA sequencing, as well as flow cytometry, IHC, and qRT-PCR, studies showed
253 marked T cell thyroid infiltration with ICI treatment (**Fig. 3a, c, and e**). Therefore, we sub-clustered
254 *Cd3e*⁺ cells to further delineate the T cell populations present and their functional status (**Fig. 3f**,
255 *n*=3,178 cells). This identified 10 populations including CD4⁺ (clusters 0,1,4,7), CD8⁺ (2), mixed
256 CD4⁺ and 8⁺ (8,9) and TCR $\gamma\delta$ ⁺ (3,5,6) subsets (**Fig. 3f, Extended Data Fig. 4c, and Extended**
257 **Data Table 1**). Thyroid tissue infiltrating T cells showed gene expression associated with
258 activation (*Cd44*, *Cd69*) and effector functions, including type 1 (*Tbx21*) and type 3 (*Rorc*)
259 immunity and cytotoxicity (T cell subcluster 2: *Cd8a*, *Cd8b*, *Gzmk*, *Ccl5*, *Fasl*, *Prf1*, *Klrd1*, *Klrc1*,
260 *Gzmk*, *Ly6a*, *Eomes*; and subcluster 6: *Ncr1*, *Trdc*, *Klra5*, *Klra4*, *Klra1*, *Klrd1*, *Cd7*, *Nkg7*). Type
261 1 immunity and cytotoxic T cells have previously been reported in ICI treatment and are thought
262 to be important for anti-tumor effects^{36,46}. However, a role for Type 3 immune responses in ICI
263 treatment is less clear.

264

265 *RORc* expression, associated with Type 3 immunity, was highest in subclusters 3 and 5 (**Fig. 3g**).
266 Both *Rorc*⁺ clusters also coordinately expressed *Trdc*, *Tcr γ -V6*, *Rora*, *Tmem1276b*, *Tmem176a*,
267 *Cxcr6*, and *Serpinb1a*, supporting their inclusion of $\gamma\delta$ T17 cells (**Extended Data Fig. 4c and**
268 **Extended Data Table 1**)⁴⁷. We confirmed increased expression of *Rorc* and associated
269 Th17/ $\gamma\delta$ T17 pathway genes *Il23r* and *Il17a* using qRT-PCR. As shown in **Fig. 3h**, expression was

270 significantly increased in ICI-treated vs. isotype mice for *Rorc* [mean fold change (FC) 2.4±0.1,
271 p<0.001], *Il23r* (FC 1.28±0.09, p<0.001), and *Il17a* (FC 1.45±0.07, p<0.001)]. In addition, flow
272 cytometry analysis of infiltrating immune cells dissociated from fresh thyroid showed increased
273 intrathyroidal ROR γ T⁺ pan-CD3⁺ T cells, which include Th17 and γ δ T17 cells, in Dual ICI-treated
274 mice compared to isotype controls (mean 936±267 vs. 183±43 cells per thyroid lobe, **Fig. 3i**).
275 These data, together with our earlier data that Th17 and γ δ T17 cells were increased in the spleen
276 of ICI-treated mice (**Fig. 2**), suggest a potential role for ROR γ T⁺ Th17 and/or γ δ T17 cells in the
277 development of ICI-associated thyroiditis.

278
279 To better characterize the ROR γ T⁺ populations in thyroid immune infiltrates, we sub-clustered T
280 cells with detectable ROR γ T expression (*Rorc* > 1) (**Fig. 4a** and **Extended Data Fig. 4e**). This
281 analysis produced 3 subclusters (0,1,2): Subclusters 0, 1, and 2 expressed high levels of γ δ T cell
282 markers (*Trdc*, *Trg-V6*), and Subcluster 2 also included CD4⁺ T helper cells (*Cd4*). Subclusters 0
283 and 1 differentially expressed *Il23r* (**Fig. 4b**), suggesting two γ δ T17 cell states that could be
284 distinguished by *Il23r*. Moreover, *Pdcd1* was expressed by all three subclusters and *Ctla4* was
285 highly expressed by Subcluster 2, which suggests that all three subclusters can be activated by
286 anti-PD1 and/or anti-CTLA-4 checkpoint inhibitors (**Fig. 4c**). We also queried the expression of
287 cytokine receptors previously reported to promote induction of γ δ T17 cells, namely *Tnfrsf1a* and
288 *Il1r1*⁴². Subclusters 0 and 1 expressed the highest levels of *Tnfrsf1a*, while Subclusters 0, 1, and
289 2 each expressed *Il1r1* (**Fig. 4d**). Thus, cytokine receptors needed for γ δ T17 differentiation are
290 indeed present in these ROR γ T⁺ T cells. In support of an important role for TNF α and IL-1 β in γ δ T17
291 cell induction, intrathyroidal myeloid cells strongly expressed inflammatory cytokine genes *Tnf*
292 and *Il1b* (**Extended Data Fig. 5a-c**) in scRNAseq data. Increased intrathyroidal TNF α and IL-1 β
293 was confirmed using qRT-PCR comparing ICI-treated to isotype mice (**Extended Data Fig. 5d**).
294 Of note, TNF α and IL-1 β also amplifies Th17 differentiation⁴⁸, and additional cytokines associated

295 with Th17 development (TGF β and IL-6) were also increased, although to a lesser degree, in
296 thyroids of ICI-treated mice (**Extended Data Fig. 5c-d**)³⁸. Finally, predicted ligand-receptor
297 interactions in scRNAseq data showed significant cell-cell communication from myeloid
298 populations to T cells via CXCL and CCL family chemokines (**Extended Data Fig. 5e and**
299 **Extended Data Table 2**). Interestingly, CXCL communication arose singularly from the predicted
300 interaction of myeloid chemokine CCL16 with T cell CXCR6. CXCR6 was highly expressed on
301 *RORc*⁺ T cells and has been associated with Th17 and $\gamma\delta$ T17 cell recruitment⁴⁹. Together, these
302 data suggest a model in which intrathyroidal $\gamma\delta$ T17 and Th17 activation and induction can occur
303 through: i) binding of PD-1 and CTLA-4 by checkpoint inhibitors, and ii) pro-inflammatory cytokine
304 and chemokine signaling.

305

306 *RORc* encodes ROR γ t, a master transcriptional regulator that drives expression of IL-17 cytokines
307 in multiple cell types^{50,51}. Consistent with thyroid infiltration of *Rorc*⁺ immune cells,
308 immunohistochemical staining showed increased IL-17A in thyroid tissue of Dual ICI-treated mice
309 compared to isotype control-treated mice (**Fig. 4e**). Furthermore, flow cytometric analysis of
310 dissociated thyroid tissue showed increasing numbers of IL-17A-producing $\gamma\delta$ T17 and Th17 cells
311 in ICI-treated mice from 1 to 4 weeks after ICI initiation (**Fig. 4f-g**). IL-17A-producing CD4⁻ $\gamma\delta$ TCR⁻
312 T cells were also seen and may represent ILC3 or CD8⁺ Tc17 cells^{52,53}. Combination ICI therapy
313 produced the greatest infiltration of $\gamma\delta$ T17 and Th17 cells, followed by single agent anti-PD-1 and
314 anti-CTLA-4 treatment (**Fig. 4g**). IL-17A⁺ $\gamma\delta$ T cells were also predominantly CD27⁻ and CD44⁺
315 (**Fig. 4h**), consistent with scRNAseq data from thyroid infiltrating immune cells and the previously
316 reported phenotype of $\gamma\delta$ T17 cells^{54,55}. Together these data strongly implicate a role for IL-17A⁺
317 ROR γ t⁺ Th17 and $\gamma\delta$ T17 cells in the development of ICI-thyroiditis.

318

319 Finally, we sought to identify cellular targets of IL17A, which binds to and signals through
320 IL17RA/IL17RC heterodimers. IL17RA is widely expressed in the body and alone considered
321 insufficient for strong IL-17A signal transduction⁵⁶. IL-17 receptor C (IL-17RC), the necessary
322 binding partner of IL-17RA for IL-17A signaling (**Extended Data Fig. 6a**), is more selectively
323 expressed⁵⁶. Evaluation of thyroid-infiltrating immune cells (CD45⁺) by scRNAseq studies did not
324 show significant expression of IL-17RC (data not shown). However, IL-17RC was expressed on
325 thyroid epithelium in our mouse model by IHC (**Extended Data Fig. 6a**). In addition, we evaluated
326 IL-17RC gene expression on NThy-Ori-3.1 cells, an SV-40 transformed human thyroid epithelial
327 cell line routinely used to study normal thyroid cell function, by qRT-PCR (**Extended Data Fig.**
328 **6b**). NThy-Ori-3.1 cells expressed 4-fold more IL-17RC than 293T cells, a model of human
329 embryonic kidney used as a reference tissue ($p < 0.05$). IL-17A signaling through IL-17RA/RC can
330 induce apoptosis^{57,58}. These findings are consistent with a previous report that thyroid follicular
331 epithelial cells express high levels of IL-17RC⁵⁹ and suggest that IL17A may directly target thyroid
332 cells.

333

334 ***IL-17A neutralizing antibody reduces autoimmune infiltrates in ICI-treated mice***

335 Based on these data, we predicted that blocking IL-17A could reduce thyroid autoimmunity in ICI-
336 treated mice. We therefore tested the effects of an IL-17A neutralizing antibody (clone 17F3,
337 0.5mg/dose 3x/week *i.p.*) 10 days after Dual ICI therapy in NOD mice (**Fig. 5a**). Indeed, this IL-
338 17A neutralizing antibody reduced the frequency and severity of autoimmune infiltrates in ICI-
339 treated mice at 4 weeks, including thyroiditis (**Fig. 5b-c**; ANOVA $p < 0.0001$, pairwise comparisons
340 vs. Dual ICI $p < 0.001$ for isotype, Dual ICI + α IL-17A, and Dual + α TNF α). Specifically, thyroid
341 infiltrating CD45⁺ immune cells were reduced from mean 16,543 \pm SEM 7,940 cells/lobe in Dual
342 ICI-treated mice, to 339 \pm 133 in Dual ICI with anti-IL17A, and compared to 1,406 \pm 872 in isotype-
343 treated mice (ANOVA $p < 0.03$; p values vs. Dual ICI were isotype 0.2, Dual + α IL17A 0.16, and

344 Dual + α TNF α CD45⁺ 0.26). Thyroid-infiltrating CD3⁺(α β and γ δ TCR) T cells were reduced as
345 well, mean 3,418 \pm 1,271 cells/thyroid lobe in Dual ICI vs. 164 \pm 59 with Dual ICI + anti-IL17A vs.
346 478 \pm 207 with isotype (ANOVA p=0.01; p values for pairwise comparisons vs. Dual ICI were
347 isotype 0.09, Dual + α IL17A 0.05, and Dual + α TNF α CD45⁺ 0.36). Dual ICI + anti-IL-17A). Other
348 thyroid-infiltrating immune cell populations evaluated were also decreased, including B cells
349 (mean 212 \pm 77 cells/thyroid lobe in Dual ICI vs. 20 \pm 10 in Dual ICI + anti-IL17A vs. 32 \pm 13 in
350 isotype, ANOVA p=0.01; p values vs. Dual ICI were isotype 0.08, Dual + α IL17A 0.06, Dual +
351 α TNF α 0.10), NK cells (mean 222 \pm 75 cells/thyroid lobe in Dual ICI vs. 16 \pm 4 in Dual ICI + anti-
352 IL17A vs. 46 \pm 16 in isotype, ANOVA p<0.001; p values vs. Dual ICI were isotype 0.09, Dual +
353 α IL17A 0.04, and Dual + α TNF α 0.04), CD11c⁺CD11b^{low} DC (mean 42 \pm 9 cells/thyroid lobe in
354 Dual ICI vs. 8 \pm 2 in Dual ICI + anti-IL17A vs. 11 \pm 3 in isotype, ANOVA p<0.001; p values vs. Dual
355 ICI were isotype 0.008, Dual + α IL17A 0.005, and Dual + α TNF α 0.002), and CD11c⁺CD11b⁺ DC
356 (mean 214 \pm 39 cells/thyroid lobe in Dual ICI vs. 46 \pm 10 in Dual ICI + anti-IL17A vs. 67 \pm 13 in
357 isotype, ANOVA p<0.001; p values vs. Dual ICI were isotype 0.006, Dual + α IL17A 0.002, and
358 Dual + α TNF α 0.0004). Controls treated with isotype + IL17A inhibitor showed infiltrates
359 comparable to isotype-only controls (data not shown). Interestingly, anti-IL-17A did not
360 significantly reduce thyroid autoantibodies against TPO or Tg (**Fig. 5d**), suggesting that ICI-
361 associated autoantibody production may be independent from thyroid immune infiltration.

362

363 Our data also showed thyroid accumulation of macrophages and monocytes that express TNF α ,
364 a pro-inflammatory cytokine important in the differentiation of γ δ T17 and Th17 cells^{42,48} (**Extended**
365 **Data Fig. 5a-c**). Interestingly TNF α has previously been implicated in patients with ICI-associated
366 colitis; Perez-ruiz *et al.*²² showed that prophylactic TNF α blockade reduced the incidence of colitis
367 during ICI therapy in a mouse model. Given its role in the IL-17A axis and efficacy in preventing
368 ICI-associated colitis, we also evaluated the effects of a TNF α neutralizing antibody (clone

369 XT3.11, 0.4mg/dose 3x/week *i.p.*) begun 10 days after anti-PD-1 + anti-CTLA-4 ICI therapy (**Fig.**
370 **5a**). A TNF α neutralizing antibody significantly reduced immune infiltrates across multiple tissues
371 in our mouse model of ICI-associated autoimmunity (**Fig. 5b**) and reduced thyroid autoimmune
372 cell infiltrates (**Fig. 5c**). Thyroid autoantibodies against TPO and Tg were not significantly
373 changed by TNF α neutralizing antibody treatment (**Fig. 5d**). Thus, inhibition of the IL-17A axis
374 (via IL-17A or TNF α blockade) effectively prevents IRAE development with ICI treatment.

375

376 ***IL-17A neutralizing antibody during ICI treatment does not reduce anti-tumor effects***

377 Our data in ICI-treated NOD mice suggested that a neutralizing IL-17A antibody may reduce IrAE,
378 including ICI-thyroiditis. In developing therapies to prevent or reduce IrAE in patients, it will be
379 critical that any approach preserve or enhance the anti-tumor immune effects of ICI. Recent data
380 from gut IrAE showed that prophylactic TNF α inhibition with a neutralizing antibody during ICI
381 treatment of murine colon cancer model MC38 did not significantly reduce anti-cancer efficacy,
382 as assessed by tumor growth curves and tumor infiltrating effector T cells²². Whether IL-17A
383 inhibition will have deleterious effects on the efficacy of ICI treatment in anti-tumor immunity is
384 unclear, since IL-17A has been associated with pro-tumorigenic effects in some cancers^{44,60,61}
385 and anti-tumorigenic effects in others^{44,60,61}. To test this, we determined the effect of IL-17A
386 blockade during ICI treatment on the growth of MC38 tumor cells; this model was selected due to
387 lack of available tumor models in the NOD strain. As expected, dual ICI treatment of MC38 tumors
388 in B6 mice significantly reduced tumor growth (**Fig. 5e**). Importantly, the addition of an IL-17A
389 neutralizing antibody did not reduce the anti-tumor effect of ICI treatment and showed a trend
390 toward improved anti-tumor effects (**Fig. 5e**; ANOVA for day 22 tumor volume $p < 0.05$; p values
391 for comparison to isotype were Dual ICI 0.0337, Dual ICI + α IL-17A 0.008, and α IL-17A 0.051.
392 No significant difference between Dual ICI vs. Dual ICI + α IL-17A, $p = 0.9$). In summary, blockade

393 of IL-17A function by a neutralizing antibody begun after ICI treatment significantly reduced IrAE
394 while preserving anti-tumor efficacy of anti-PD-1 + anti-CTLA-4 therapy.

395

396 ***Increased circulating IL-17A⁺ T cells in ICI-treated patients with thyroid IrAE***

397 To correlate our findings in mice to humans, we evaluated blood samples of patients with cancer
398 treated with ICI therapy who developed thyroid IrAE and compared them to subjects with
399 spontaneous thyroid autoimmunity (*i.e.* Hashimoto's thyroiditis, HT) or no thyroid disease (healthy
400 controls). Consistent with published reports, IL-17A⁺ CD3⁺, CD4⁺ and $\gamma\delta$ T cells showed a trend
401 for increased frequency in patients with HT compared to controls^{40,41}. Furthermore, patients
402 treated with ICI showed a trend toward increased IL-17A⁺ pan-CD3⁺ ($\alpha\beta$ and $\gamma\delta$) cells in peripheral
403 blood (**Fig. 6a and Extended Data Fig. 7**). While CD4⁺ Th17 cells showed a trend toward
404 increase, $\gamma\delta$ T17 cells were significantly increased in ICI-treated patients compared to healthy
405 controls ($p < 0.05$).

406

407 **DISCUSSION**

408 Immune checkpoint inhibitors (anti-PD-1/L1 and anti-CTLA-4) have significantly advanced the
409 treatment of cancer since their first approval in 2011. However, the benefits and use of ICI have
410 been limited by the frequent development of unwanted IrAE that contribute to patient morbidity
411 and may lead to interruption of cancer treatment. Despite significant efforts to date, the cause of
412 IrAE remained poorly understood. Using a novel mouse model in which checkpoint inhibitor
413 therapy leads to multi-organ autoimmune infiltrates, we identify Type 3 immune cells including
414 Th17 and $\gamma\delta$ T17 cells as critical contributors to IrAE development in this model (**Fig. 6b**). PD-1
415 and CTLA-4 are expressed by these immune cell subsets, suggesting that they may be direct
416 targets of ICI. Furthermore, the thyroid microenvironment of ICI-treated mice is replete with TNF α ,
417 IL1 β , and other inflammatory cytokines that promote Th17 and $\gamma\delta$ T17 cell activation and induction.

418 Indeed, antibody-based inhibition of IL17A and TNF α protected mice from ICI-induced
419 autoimmunity. Finally, IL-17A neutralization with ICI treatment in a tumor model did not reduce
420 ICI anti-tumor efficacy and indeed showed a trend toward enhancement. Thus, targeting type 3
421 immune cells in ICI-treated patients may reduce IrAE without impairing the anti-tumor efficacy of
422 ICI.

423

424 In our model, ICI-treated NOD mice developed thyroiditis comprised of a T cell predominant but
425 diverse immune infiltrate. Angell *et al.* first reported on the thyroid immune cell infiltrate in a patient
426 with ICI-thyroiditis, noting lymphocytic cells and histiocytes¹⁴. In a subsequent study, Kotwal *et*
427 *al.*⁶² evaluated immune cells in thyroid FNA specimens from eight ICI-thyroiditis patients and
428 noted a predominant CD3⁺ T cell population, as well as myeloid cells. Interestingly, they noted a
429 significantly increased CD4⁻ CD8⁻ CD3⁺ T cell population in ICI-thyroiditis patients compared to
430 healthy controls (1.9% vs. 0.7% of CD45⁺ cells), though these were not characterized as $\gamma\delta$ T
431 cells. This study also demonstrated an increase in PD-1⁺ T cells in thyroid immune infiltrates
432 compared to healthy controls that is similar to our findings of increased checkpoint protein (PD-1
433 and CTLA-4) expression on thyroid-infiltrating ROR γ t⁺ T cells in ICI-treated mice. Finally, a recent
434 report by Yasuda *et al.*²⁶ evaluating anti-PD-1 therapy in mice pre-immunized with human
435 thyroglobulin, showed a key role for CD4⁺ T cells in the development of ICI-associated thyroiditis.
436 While our results are consistent with this, our studies further demonstrate the importance of Th17
437 subsets within CD4⁺ T cells as well as non-CD4⁺ $\gamma\delta$ T17 subsets.

438

439 While Th17 cells are well described in spontaneous autoimmunity, including Hashimoto's
440 thyroiditis, they have not previously been reported in IrAE. $\gamma\delta$ T17 cells, in contrast, have not
441 previously been described in studies of spontaneous thyroiditis or in IrAE⁶³. $\gamma\delta$ T17 cells are unique
442 in their early activation and robust cytokine production compared to $\alpha\beta$ TCR T cells^{42,43,64}. Given

443 this, $\gamma\delta$ T17 cells may underlie the rapid onset that characterizes thyroid IrAEs compared to
444 spontaneous autoimmune thyroiditis. Because $\gamma\delta$ T17 cells have been reported to expand Th17
445 cells, early $\gamma\delta$ T17 activation with checkpoint inhibition in combination with inflammatory cytokines
446 (e.g. IL-1 β and TNF α) from myeloid cells may drive activation and recruitment of Th17, CD8⁺, and
447 other T cell populations. Furthermore, other IL-17A producing immune cells, namely ILC3, may
448 also contribute to autoimmunity during ICI treatment and this possibility warrants further study.

449

450 The IrAE predisposition of the inbred NOD strain may mimic humans with genetic predisposition
451 to IrAE development. For instance, HLADR15 haplotype has been associated with pituitary IrAE⁶⁵
452 while the HLADR4 haplotypes has been associated with autoimmune diabetes IrAE in humans²⁰.
453 Autoimmune predisposition has been mapped to NOD polymorphic regions which include MHC.
454 This model using NOD mice overcomes some critical limitations of previous models that required
455 deletion of regulatory populations, transfection of human checkpoint proteins, or the requirement
456 for chemical stimulants or xeno-antigen immunization for autoimmunity²²⁻²⁶. For instance,
457 NOD.H2h4 mice, which have been used previously to study thyroiditis^{39,66,67} and anti-CTLA-4
458 induced thyroiditis²⁵, require excess dietary Nal to precipitate thyroiditis via follicular cell injury
459 and TNF α stimulation, have high background rates of thyroiditis (100% after 6 weeks of Nal
460 supplementation⁶⁶), and are confounded by the presence of a non-syngeneic MHC class II
461 molecule^{27,66}. In contrast, our model in NOD mice provides an immune competent system with
462 low rates of spontaneous autoimmunity at advanced age, more similar to the background human
463 population. As seen in humans, mice with a genetic predisposition (*i.e.* NOD vs. B6) developed
464 more IrAE across multiple tissues following ICI treatment and with combination vs. single agent
465 ICI therapy^{20,31}.

466

467 IrAE remain a significant barrier to the use of ICI but therapeutic strategies to prevent IrAEs have
468 not been widely implemented. A primary consideration in the development of strategies to reduce
469 IrAE must be the preservation of anti-cancer effects of ICI. Early efforts using glucocorticoids for
470 IrAE treatment inconsistently reversed autoimmunity or compromised anti-cancer effects^{5,19}. In
471 addition, previous studies have shown reduction of thyroid IrAE by elimination of CD4⁺ T cells²⁶,
472 but this is not readily translatable to cancer patients given the importance of CD4⁺ T cells in cell-
473 mediated immunity^{36,68}. Similarly, while Tbet1⁺ IFN γ -producing T cells are seen in thyroid immune
474 infiltrates and almost certainly contribute to autoimmunity⁶⁹, these cells are known to be critical to
475 anti-cancer effects of ICI^{46,70,71} and therefore cannot feasibly be inhibited for IrAE prevention.
476 Here, we provide additional evidence that TNF blockade may prevent IrAE²² and also suggest
477 that IL-17 blockade may be useful. Both targets have therapies that are already FDA approved.
478 While focused on thyroid IrAE, a common autoimmune side effect encountered during ICI
479 treatment that results in permanent organ dysfunction, these mechanisms may be shared among
480 IrAE in other organs with more grave clinical consequences. ICI-associated colitis has been
481 associated with increased circulating IL-17A in patients treated with anti-CTLA-4^{72,73}. Mice in our
482 model developed multi-organ autoimmunity, including colitis, pneumonitis, hepatitis, and
483 nephritis, and therefore can be used to study IrAE in these organs. Furthermore, neutralizing IL-
484 17A antibody therapy decreased overall autoimmune infiltrates, including in non-thyroid tissues,
485 and therefore may be of utility in reducing IrAE during ICI more broadly. Based upon these results,
486 and the prior important work of others²², we propose that a clinical trial evaluating inhibition of the
487 IL-17A axis for prevention of IrAE in patients with cancer receiving ICI treatment should be
488 pursued.

489

490 **Tables**

491 None

492

493 **Figure Legends**

494 **Figure 1. ICI therapy induces multi-system autoimmune infiltrates (IrAE) in B6 and NOD**
495 **mice.**

496 **a**, Schematic of ICI drug treatment. **b**, Comparison of autoimmune organ infiltration after 4 weeks
497 of ICI vs. isotype treatment in C57/B6 (B6) mice ($n=8$ isotype, $n=8$ Dual ICI); Pie charts (*right*)
498 show tissue infiltrate for each mouse; black = immune infiltrate, white = no infiltrate, gray = no
499 data. **c**, Quantification of anti-thyroid autoantibodies in B6 mice after 4 weeks of isotype ($n=8$) or
500 Dual ICI ($n=8$) treatment. **d**, Comparison of autoimmune organ infiltration after 8 weeks of ICI
501 treatment in NOD mice ($n=12$ isotype, $n=11$ anti-CTLA-4, $n=11$ anti-PD-1, and $n=13$ Dual ICI).
502 Pie charts show tissue infiltrate for each mouse, as in **b** above. **e**, Representative H&E
503 micrographs of autoimmune tissue infiltrates in Dual ICI vs. isotype treated mice (original mag.
504 100x). **f**, Quantification of anti-thyroid autoantibodies in NOD mice after 8 weeks of treatment
505 ($n=10$ isotype anti-Tg or 13 for anti-TPO, $n=12$ anti-CTLA-4, $n=11$ anti-PD-1, and $n=13$ Dual ICI
506 for anti-Tg or 22 for anti-TPO). **g**, Free thyroxine serum levels in ICI-treated NOD mice after 8
507 weeks of treatment. Data are mean \pm SEM. * $p<0.05$, ** $p<0.01$, *** $p<0.001$, unpaired t test, two-
508 tailed (**b,c**), Brown-Forsythe ANOVA, assuming unequal s.d., followed by Dunnett's multiple
509 comparisons test (**d,g**), or one-way ANOVA and Dunnett's multiple comparison test (**f**).

510

511 **Figure 2. Flow cytometry analysis of peripheral immune changes in ICI-treated NOD mice.**

512 **a**, Frequency of CD3⁺ T (CD3⁺ NKp46⁻) cells in spleen in isotype ($n=7$) vs. anti-PD-1 + anti-CTLA-
513 4 (Dual ICI, $n=8$) NOD mice after 4 weeks. **b**, Relative frequency of activated T cells (CD44⁺
514 CD62L⁻) among CD4⁺ and CD8⁺ T cell subsets in spleen in isotype ($n=7$ or 8) and Dual ICI ($n=8$
515 or 10). **c**, Relative frequency of interferon (IFN)- γ ⁺ cells within CD4⁺ population between isotype

516 ($n=7$) and Dual ICI-treated ($n=8$) mice. **d**, Relative frequency of IL-17A⁺ cells in CD4⁺ pop.
517 between isotype ($n=14$) and Dual ICI-treated ($n=14$) mice. **e**, Representative histogram of ROR γ t⁺
518 by thyroid-infiltrating CD4⁺ cells from isotype vs. ICI-treated mice; 7 ICI treated and 8 isotype mice
519 evaluated. **f**, Gating strategy for CD4⁺ and IL-17A⁺ populations from spleen, and relative
520 frequency of CD4⁺ and CD4⁻ IL-17A⁺ cells in spleen from isotype ($n=12$) and Dual ICI-treated
521 ($n=10$) mice. **g**, Frequency of IL-17A⁺ cells within gamma delta ($\gamma\delta$) cells in spleen from isotype
522 ($n=12$) and Dual ICI-treated ($n=10$) mice. Data are mean. * $p<0.05$, two-tailed, unpaired t test with
523 Welch correction, assuming unequal s.d., and Holm-Sidak method correction for multiple
524 comparisons (**a-d,f,g**).

525

526 **Figure 3. Characterization of thyroid-infiltrating immune cells in ICI-treated NOD mice.**

527 **a**, IHC staining for T cells (CD3), macrophages (F4/80), and B cells (B220) in thyroid tissue from
528 Dual ICI- ($n=7, 10$, or 9) vs. isotype- ($n=4$) treated mice [*left*, representative sections, 400x original
529 mag.; *right*, cells/hpf]. **b**, Representative gating strategies and dot plots (*left*) and relative
530 frequency of CD45⁺ immune cells in thyroid tissue (*right*, cells per thyroid lobe) from isotype ($n=11$)
531 vs. Dual ICI ($n=17$) treated mice after 4 weeks. **c**, Relative frequency of immune subpopulations
532 in isotype ($n=11$, except $n=16$ for CD3⁺ and B220⁺) vs. Dual ICI-treated ($n=17$, except $n=23$ for
533 CD3⁺ and B220⁺) mice. **d**, Schematic of tissue processing for single cell RNA sequencing (*left*).
534 UMAP plot of 4,095 thyroid-infiltrating CD45⁺ immune cells from 10 pooled Dual ICI-treated mice,
535 2 independent experiments (*right*). Cluster analysis yields 14 distinct clusters comprising CD4,
536 CD8, and $\gamma\delta$ T cells, natural killer (NK)/NKT cells, innate lymphoid cells (ILC), B cells,
537 macrophages, and dendritic (DC)/antigen presenting cells (APC). **e**, Intrathyroidal gene
538 expression for *Cd45* and *Cd3e* in ICI-treated vs. isotype mice measured by qRT-PCR. **f**, UMAP
539 of CD3-subclustered cells, $n= 3,178$ cells. Cluster analysis yields 10 distinct clusters comprising
540 CD4, CD8, and $\gamma\delta$ T cells (*left*). Feature and violin plots for T cell subset markers for $\delta\gamma$ (*Trdc*),

541 CD4 (*Cd4*), and CD8 (*Cd8a*) (*right*). **g**, Violin plots for type 3 immunity (ROR γ t-pathway)
542 associated genes *Rorc* and *Il23r*. **h**, Intrathyroidal gene expression for *Rorc*, *Il23r*, and *Il17a* in
543 ICI-treated vs. isotype mice, by qRT-PCR. **i**, Comparison of thyroid-infiltrating ROR γ t⁺ pan-CD3⁺
544 ($\alpha\beta$ and $\gamma\delta$) T cells by flow cytometry in ICI-treated (*n*=8) vs. isotype (*n*=6) mice. Data are
545 mean \pm SEM. For qRT-PCR, mean fold change \pm SEM, *n*=12 animals/group; thyroid tissue pooled
546 and run in 3 experiments, in triplicate. **p*<0.05, ***p*<0.01, two-tailed, unpaired t test with Welch
547 correction, assuming unequal s.d. (**a-c,i**) and Holm-Sidak method correction for multiple
548 comparisons (**e,h**).

549

550 **Figure 4. ROR γ t⁺ IL-17A⁺ T cells in thyroid immune infiltrates of ICI-treated mice.**

551 **a**, UMAP of *Rorc*-subclustered cells, *n*=361 cells. Cluster analysis yields 3 distinct clusters (*left*)
552 comprised of CD4 and $\gamma\delta$ T cells, as shown by violin plots (*right*). **b**, Feature and violin plots for
553 Th17- and $\gamma\delta$ T17-associated genes. **c-d**, Violin plots for checkpoint proteins (**c**) *Pdcd1* and *Ctla4*
554 and inflammatory cytokine receptors (**d**) *Tnfrsf1a* and *Il1r1* on *Rorc*⁺ thyroid-infiltrating T cells. **e**,
555 IHC staining for IL-17A in thyroid tissue of isotype and Dual ICI-treated mice (representative
556 sections from 3 independent experiments, original mag. 400x). **f**, Gating strategy and
557 representative dot plots of IL-17A⁺ CD4⁺ (Th17) and $\gamma\delta$ ⁺ ($\gamma\delta$ T17) cells in thyroid immune infiltrates
558 in isotype or Dual ICI-treated mice at 1-4 weeks (*n*=2 pooled animals each condition). **g**,
559 Quantification of intrathyroidal CD4⁺ IL-17A⁺ and TCR $\gamma\delta$ ⁺ IL-17A⁺ cells from thyroid immune
560 infiltrates from ICI-treated mice at different timepoints of ICI-thyroiditis development. **h**,
561 Representative gating strategy and flow cytometry dot plots showing CD44⁺ and CD27⁻ phenotype
562 of TCR $\gamma\delta$ ⁺ IL-17A⁺ cells. **g-h**, for plots shown, pooled thyroid immune infiltrates from isotype (*n*=2),
563 anti-PD-1 (*n*=3), anti-CTLA-4 (*n*=4), and Dual ICI (*n*=2) treated mice after 4 weeks, or sooner
564 timepoints (*n*=2) from Dual ICI treated for Time Course.

565

566 **Figure 5. Neutralizing IL-17A or TNF α antibody reduces anti-PD-1 + anti-CTLA-4 (Dual**
567 **ICI)-associated autoimmune infiltrates.**

568 **a**, Schematic of treatment regimen. **b**, Autoimmune organ infiltrate score after 4 weeks of ICI
569 treatment in isotype ($n=14$), Dual ICI ($n=16$), Dual ICI + neutralizing IL-17A antibody (α IL17A,
570 $n=7$), and Dual ICI + neutralizing TNF α antibody (α TNF α , $n=8$). Pie charts (*right*) showing tissues
571 with immune infiltration after 4 weeks of ICI treatment. Each pie represents one animal; black =
572 immune infiltrate, white = no infiltrate, gray = no data. **c**, Intrathyroidal immune cell frequency
573 among groups [isotype, $n=11$, except $n=16$ for CD3 $^+$], Dual ICI ($n=17$, except $n=23$ for CD3 $^+$),
574 Dual ICI + α IL17A ($n=8$), Dual ICI + α TNF α ($n=8$)]. **d**, Anti-thyroid autoantibodies in NOD mice
575 after 4 weeks of treatment with isotype ($n=14$ for anti-TPO, $n=12$ for anti-Tg), Dual ICI ($n=18$ for
576 anti-TPO, $n=13$ for anti-Tg), Dual ICI + α IL17A ($n=8$), Dual ICI + α TNF α ($n=8$). **e**, Growth of MC38
577 tumors in B6 mice treated with anti-PD-1 + anti-CTLA-4 (Dual ICI) or isotype control, as well as a
578 neutralizing IL-17A (α IL17A) or relevant isotype, time ($n=6$ each group). Data are mean \pm SEM
579 shown. ** $p<0.01$, *** $p<0.001$, **** $p<0.0001$. Brown-Forsythe ANOVA, assuming unequal s.d.,
580 followed by Dunnett's multiple comparisons test as indicated (**b-d**), or ANOVA for tumor volume
581 at day 22, followed by Dunnett's multiple comparisons test (**e**).

582

583 **Figure 6. $\gamma\delta$ T17 and Th17 cells in ICI-treated cancer patients.**

584 **a**, Relative frequency of IL-17A $^+$ pan-CD3 $^+$, Th17, and $\gamma\delta$ T17 cells in peripheral blood of controls
585 ($n=6$), patients with Hashimoto's thyroiditis (HT, $n=13$), or patients with cancer treated with ICI
586 ($n=20$). Mean shown. * $p<0.05$. Brown-Forsythe ANOVA, assuming unequal s.d., followed by
587 Dunnett's multiple comparisons test. **b**, Proposed mechanism of Thyroid IrAE. (1) ROR γ t $^+$ Th17
588 and $\gamma\delta$ T17 cells may be activated by anti-PD-1 and/or anti-CTLA-4 inhibitor binding to (2) release
589 IL-17A. (3) In addition, myeloid cells within the thyroid may contribute to Th17 and $\gamma\delta$ T17 activation
590 and recruitment by production inflammatory cytokines IL-1 β and TNF α and chemokines. IL-17A

591 within the thyroid microenvironment may affect thyroid follicular cell death via (4) induction of
592 apoptosis or indirectly by (5) facilitating the accumulation of cytotoxic effector cells. (6) Strategies
593 to reduce IrAE target the IL-17A axis.

594

595 **References Cited**

- 596 1. Wei, S. C., Duffy, C. R. & Allison, J. P. Fundamental mechanisms of immune checkpoint
597 blockade therapy. *Cancer Discov.* **8**, 1069–1086 (2018).
- 598 2. Haslam, A. & Prasad, V. Estimation of the Percentage of US Patients With Cancer Who
599 Are Eligible for and Respond to Checkpoint Inhibitor Immunotherapy Drugs. *JAMA Netw.*
600 *open* **2**, e192535 (2019).
- 601 3. Larkin, J. *et al.* Five-year survival with combined nivolumab and ipilimumab in advanced
602 melanoma. *N. Engl. J. Med.* **381**, 1535–1546 (2019).
- 603 4. Arnaud-Coffin, P. *et al.* A systematic review of adverse events in randomized trials
604 assessing immune checkpoint inhibitors. *International Journal of Cancer* vol. 145 639–
605 648 (2019).
- 606 5. Das, S. & Johnson, D. B. Immune-related adverse events and anti-tumor efficacy of
607 immune checkpoint inhibitors. *J. Immunother. Cancer* **7**, 1–11 (2019).
- 608 6. De Filette, J., Andreescu, C. E., Cools, F., Bravenboer, B. & Velkeniers, B. A Systematic
609 Review and Meta-Analysis of Endocrine-Related Adverse Events Associated with
610 Immune Checkpoint Inhibitors. *Hormone and Metabolic Research* vol. 51 145–156
611 (2019).
- 612 7. Wang, D. Y. *et al.* Fatal Toxic Effects Associated With Immune Checkpoint Inhibitors: A
613 Systematic Review and Meta-analysis. *JAMA Oncol.* **4**, 1721–1728 (2018).
- 614 8. Young, A., Quandt, Z. & Bluestone, J. A. The balancing act between cancer immunity and
615 autoimmunity in response to immunotherapy. *Cancer Immunol. Res.* **6**, 1445–1452
616 (2018).
- 617 9. Iyer, P. C. *et al.* Immune-Related Thyroiditis with Immune Checkpoint Inhibitors. *Thyroid*
618 **28**, 1243–1251 (2018).
- 619 10. Delivanis, D. A. *et al.* Pembrolizumab-induced thyroiditis: Comprehensive clinical review
620 and insights into underlying involved mechanisms. *J. Clin. Endocrinol. Metab.* **102**, 2770–
621 2780 (2017).
- 622 11. De Moel, E. C. *et al.* Autoantibody development under treatment with immune-checkpoint
623 inhibitors. *Cancer Immunol. Res.* **7**, 6–11 (2019).
- 624 12. Ma, C. *et al.* The impact of high-dose glucocorticoids on the outcome of immune-
625 checkpoint inhibitor-related thyroid disorders. *Cancer Immunol. Res.* **7**, 1214–1220
626 (2019).
- 627 13. Kotwal, A. *et al.* Immune Checkpoint Inhibitor-Induced Thyroiditis Is Associated with
628 Increased Intrathyroidal T Lymphocyte Subpopulations. *Thyroid* **30**, 1440–1450 (2020).
- 629 14. Angell, T. E., Min, L., Wieczorek, T. J. & Hodi, F. S. Unique cytologic features of
630 thyroiditis caused by immune checkpoint inhibitor therapy for malignant melanoma.
631 *Genes Dis.* **5**, 46–48 (2018).
- 632 15. Nakamura, Y. Biomarkers for Immune Checkpoint Inhibitor-Mediated Tumor Response
633 and Adverse Events. *Front. Med.* **6**, (2019).
- 634 16. Álvarez-Sierra, D. *et al.* Analysis of the PD-1/PD-L1 axis in human autoimmune thyroid
635 disease: Insights into pathogenesis and clues to immunotherapy associated thyroid
636 autoimmunity. *J. Autoimmun.* **103**, (2019).
- 637 17. Brahmer, J. R. *et al.* JOURNAL OF CLINICAL ONCOLOGY. *J Clin Oncol* **36**, 1714–1768
638 (2018).

- 639 18. Thompson, J. A. *et al.* NCCN Guidelines Insights: Management of Immunotherapy-
640 Related Toxicities, Version 1.2020. *J. Natl. Compr. Canc. Netw.* **18**, 230–241 (2020).
- 641 19. Adam, K., Iuga, A., Tocheva, A. S. & Mor, A. A novel mouse model for checkpoint
642 inhibitor-induced adverse events. *PLoS One* **16**, 1–14 (2021).
- 643 20. Bluestone, J. A. *et al.* Collateral damage: Insulin-dependent diabetes induced with
644 checkpoint inhibitors. in *Diabetes* vol. 67 1471–1480 (American Diabetes Association
645 Inc., 2018).
- 646 21. Faje, A. T. *et al.* High-dose glucocorticoids for the treatment of ipilimumab-induced
647 hypophysitis is associated with reduced survival in patients with melanoma. *Cancer* **124**,
648 3706–3714 (2018).
- 649 22. Perez-Ruiz, E. *et al.* Prophylactic TNF blockade uncouples efficacy and toxicity in dual
650 CTLA-4 and PD-1 immunotherapy. *Nature* vol. 569 428–432 (2019).
- 651 23. Liu, J. *et al.* Assessing immune-related adverse events of efficacious combination
652 immunotherapies in preclinical models of cancer. *Cancer Res.* **76**, 5288–5301 (2016).
- 653 24. Du, X. *et al.* Uncoupling therapeutic from immunotherapy-related adverse effects for safer
654 and effective anti-CTLA-4 antibodies in CTLA4 humanized mice. *Cell Res.* **28**, 433–447
655 (2018).
- 656 25. Sharma, R., Di Dalmazi, G. & Caturegli, P. Exacerbation of Autoimmune Thyroiditis by
657 CTLA-4 Blockade: A Role for IFN γ -Induced Indoleamine 2, 3-Dioxygenase. *Thyroid* **26**,
658 1117–1124 (2016).
- 659 26. Yasuda, Y. *et al.* CD4 + T cells are essential for the development of destructive thyroiditis
660 induced by anti – PD-1 antibody in thyroglobulin-immunized mice. **7495**, (2021).
- 661 27. McLachlan, S. M. *et al.* Genes outside the major histocompatibility complex locus are
662 linked to the development of thyroid autoantibodies and thyroiditis in NOD.H2h4 mice.
663 *Endocrinology* **158**, 702–713 (2017).
- 664 28. Quintana, F. J. & Cohen, I. R. Autoantibody patterns in diabetes-prone NOD mice and in
665 standard C57BL/6 mice. *J. Autoimmun.* **17**, 191–197 (2001).
- 666 29. Jiang, W., Anderson, M. S., Bronson, R., Mathis, D. & Benoist, C. Modifier loci condition
667 autoimmunity provoked by Aire deficiency. *J. Exp. Med.* **202**, 805–815 (2005).
- 668 30. Toi, Y. *et al.* Profiling Preexisting Antibodies in Patients Treated with Anti-PD-1 Therapy
669 for Advanced Non-Small Cell Lung Cancer. *JAMA Oncol.* **5**, 376–383 (2019).
- 670 31. Yamazaki, H. *et al.* Potential risk factors for nivolumab-induced thyroid dysfunction. *In*
671 *Vivo (Brooklyn)*. **31**, 1225–1228 (2017).
- 672 32. Anderson, M. S. & Bluestone, J. A. THE NOD MOUSE: A Model of Immune
673 Dysregulation. *Annu. Rev. Immunol.* **23**, 447–485 (2005).
- 674 33. Podolin, P. L. *et al.* I-E+ nonobese diabetic mice develop insulinitis and diabetes. *J. Exp.*
675 *Med.* **178**, 793–804 (1993).
- 676 34. Damotte, D. *et al.* Analysis of susceptibility of NOD mice to spontaneous and
677 experimentally induced thyroiditis. *Eur. J. Immunol.* **27**, 2854–2862 (1997).
- 678 35. Su, M. A. *et al.* Mechanisms of an autoimmunity syndrome in mice caused by a dominant
679 mutation in Aire. *J. Clin. Invest.* **118**, 1712–1726 (2008).
- 680 36. Oh, D. Y. *et al.* Intratumoral CD4+ T Cells Mediate Anti-tumor Cytotoxicity in Human
681 Bladder Cancer. *Cell* **181**, 1612-1625.e13 (2020).
- 682 37. Yost, K. E. *et al.* Clonal replacement of tumor-specific T cells following PD-1 blockade.
683 **25**, 1251–1259 (2020).
- 684 38. Miossec, P., Korn, T. & Kuchroo, V. K. Interleukin-17 and type 17 helper T cells. *N. Engl.*
685 *J. Med.* **361**, 888 (2009).
- 686 39. Horie, I. *et al.* T helper type 17 immune response plays an indispensable role for
687 development of iodine-induced autoimmune thyroiditis in nonobese diabetic-H2h4 mice.
688 *Endocrinology* **150**, 5135–5142 (2009).
- 689 40. Shi, Y. *et al.* Differentiation imbalance of Th1/Th17 in peripheral blood mononuclear cells

- 690 might contribute to pathogenesis of Hashimoto's thyroiditis. *Scand. J. Immunol.* **72**, 250–
691 255 (2010).
- 692 41. Konca Degertekin, C. *et al.* Circulating Th17 cytokine levels are altered in Hashimoto's
693 thyroiditis. *Cytokine* **80**, 13–17 (2016).
- 694 42. Papotto, P. H., Reinhardt, A., Prinz, I. & Silva-Santos, B. Innately versatile: $\gamma\delta$ 17 T cells in
695 inflammatory and autoimmune diseases. *J. Autoimmun.* **87**, 26–37 (2018).
- 696 43. Papotto, P. H., Ribot, J. C. & Silva-Santos, B. IL-17 + $\gamma\delta$ T cells as kick-starters of
697 inflammation. *Nat. Immunol.* **18**, 604–611 (2017).
- 698 44. Kuen, D. S., Kim, B. S. & Chung, Y. IL-17-producing cells in tumor immunity: Friends or
699 foes? *Immune Netw.* **20**, 1–20 (2020).
- 700 45. Stuart, T. *et al.* Comprehensive Integration of Single-Cell Data. *Cell* **177**, 1888-1902.e21
701 (2019).
- 702 46. Ayers, M. *et al.* IFN- γ -related mRNA profile predicts clinical response to PD-1 blockade.
703 *J. Clin. Invest.* **127**, 2930–2940 (2017).
- 704 47. Tan, L. *et al.* Single-Cell Transcriptomics Identifies the Adaptation of Scart1+ V γ 6+ T
705 Cells to Skin Residency as Activated Effector Cells. *Cell Rep.* **27**, 3657-3671.e4 (2019).
- 706 48. Veldhoen, M., Hocking, R. J., Atkins, C. J., Locksley, R. M. & Stockinger, B. TGF β in the
707 context of an inflammatory cytokine milieu supports de novo differentiation of IL-17-
708 producing T cells. *Immunity* **24**, 179–189 (2006).
- 709 49. Butcher, M. J., Wu, C. I., Waseem, T. & Galkina, E. V. CXCR6 regulates the recruitment
710 of pro-inflammatory IL-17A-producing T cells into atherosclerotic aortas. *Int. Immunol.* **28**,
711 255–261 (2016).
- 712 50. Barros-Martins, J. *et al.* Effector $\gamma\delta$ T Cell Differentiation Relies on Master but Not
713 Auxiliary Th Cell Transcription Factors. *J. Immunol.* **196**, 3642–3652 (2016).
- 714 51. Ivanov, I. I. *et al.* The orphan nuclear receptor ROR γ directs the differentiation
715 program of proinflammatory IL-17+ T helper cells. *Cell* **126**, 1121–1133 (2006).
- 716 52. Liang, Y., Pan, H. F. & Ye, D. Q. Tc17 cells in immunity and systemic autoimmunity. *Int.*
717 *Rev. Immunol.* **34**, 318–331 (2015).
- 718 53. Kuo, T.-C. *et al.* Ultrasonographic features for differentiating follicular thyroid carcinoma
719 and follicular adenoma. *Asian J. Surg.* **43**, 339–346 (2020).
- 720 54. Cai, Y. *et al.* Pivotal Role of Dermal IL-17-Producing $\gamma\delta$ T Cells in Skin Inflammation.
721 *Immunity* **35**, 596–610 (2011).
- 722 55. Markle, J. G. M. *et al.* $\gamma\delta$ T Cells Are Essential Effectors of Type 1 Diabetes in the
723 Nonobese Diabetic Mouse Model. *J. Immunol.* **190**, 5392–5401 (2013).
- 724 56. Nies, J. F. & Panzer, U. IL-17C/IL-17RE: Emergence of a Unique Axis in TH17 Biology.
725 *Front. Immunol.* **11**, 341 (2020).
- 726 57. Bockerstett, K. A. *et al.* Interleukin-17A Promotes Parietal Cell Atrophy by Inducing
727 Apoptosis. *Cmgh* **5**, 678-690.e1 (2018).
- 728 58. Su, S. *et al.* Interleukin-17A mediates cardiomyocyte apoptosis through Stat3-iNOS
729 pathway. *Biochim. Biophys. Acta - Mol. Cell Res.* **1863**, 2784–2794 (2016).
- 730 59. Uhlén, M. *et al.* Proteomics. Tissue-based map of the human proteome. *Science* **347**,
731 1260419 (2015).
- 732 60. Fabre, J. *et al.* Targeting the tumor microenvironment: The protumor effects of IL-17
733 related to cancer type. *Int. J. Mol. Sci.* **17**, (2016).
- 734 61. Zhao, J., Chen, X., Herjan, T. & Li, X. The role of interleukin-17 in tumor development
735 and progression. *J. Exp. Med.* **217**, 1–13 (2020).
- 736 62. Kotwal, A. *et al.* Immune Checkpoint Inhibitor-Induced Thyroiditis Is Associated with
737 Increased Intrathyroidal T Lymphocyte Subpopulations. *Thyroid* **00**, 1–11 (2020).
- 738 63. Paolieri, F. *et al.* Infiltrating γ/δ T-cell receptor-positive lymphocytes in Hashimoto's
739 thyroiditis, Graves' disease and papillary thyroid cancer. *J. Endocrinol. Invest.* **18**, 295–
740 298 (1995).

- 741 64. Sutton, C. E. *et al.* Interleukin-1 and IL-23 Induce Innate IL-17 Production from $\gamma\delta$ T Cells,
742 Amplifying Th17 Responses and Autoimmunity. *Immunity* **31**, 331–341 (2009).
- 743 65. Yano, S. *et al.* Human leucocyte antigen DR15, a possible predictive marker for immune
744 checkpoint inhibitor–induced secondary adrenal insufficiency. *Eur. J. Cancer* **130**, 198–
745 203 (2020).
- 746 66. Braley-Mullen, H., Sharp, G. C., Medling, B. & Tang, H. *Spontaneous Autoimmune*
747 *Thyroiditis in NOD.H-2h4 Mice*. *Journal of Autoimmunity* vol. 12
748 <http://www.idealibrary.comon> (1999).
- 749 67. McLachlan, S. M., Aliesky, H. A. & Rapoport, B. Aberrant Iodine Autoregulation Induces
750 Hypothyroidism in a Mouse Strain in the Absence of Thyroid Autoimmunity. *J. Endocr.*
751 *Soc.* **2**, 63–76 (2018).
- 752 68. Tay, R. E., Richardson, E. K. & Toh, H. C. Revisiting the role of CD4+ T cells in cancer
753 immunotherapy—new insights into old paradigms. *Cancer Gene Ther.* **28**, 5–17 (2021).
- 754 69. Horie, I., Abiru, N., Sakamoto, H., Iwakura, Y. & Nagayama, Y. Induction of autoimmune
755 thyroiditis by depletion of CD4 +CD25 + regulatory T cells in thyroiditis-resistant IL-17, but
756 not interferon- γ receptor, knockout nonobese diabetic-H2 h4 mice. *Endocrinology* **152**,
757 4448–4454 (2011).
- 758 70. Gao, J. *et al.* Loss of IFN- γ Pathway Genes in Tumor Cells as a Mechanism of
759 Resistance to Anti-CTLA-4 Therapy. *Cell* **167**, 397-404.e9 (2016).
- 760 71. Shi, L. Z. *et al.* Interdependent IL-7 and IFN- γ signalling in T-cell controls tumour
761 eradication by combined α -CTLA-4+ α -PD-1 therapy. *Nat. Commun.* **7**, (2016).
- 762 72. Tarhini, A. A. *et al.* Baseline circulating IL-17 predicts toxicity while TGF- β 1 and IL-10 are
763 prognostic of relapse in ipilimumab neoadjuvant therapy of melanoma. *J. Immunother.*
764 *Cancer* **3**, 15–20 (2015).
- 765 73. von Euw, E. *et al.* CTLA4 blockade increases Th17 cells in patients with metastatic
766 melanoma. *J. Transl. Med.* **7**, 1–13 (2009).
- 767

768 **METHODS**

769 *Mice*

770 NOD/ShiLtJ (NOD) and C57/B6 (B6) mice were obtained from the Jackson Laboratory. Male and
771 female mice were used in equal proportions unless otherwise specified. Mice were used at 4-6-
772 week of age unless otherwise noted. Mice were housed in a specific pathogen-free barrier facility
773 at the University of California Los Angeles. Diabetes, determined by presence of glucose in urine
774 (Diastix, Bayer), was assessed at least once per week and diabetic mice were treated daily with
775 intraperitoneal insulin as described previously³⁵ until used in experiments or euthanized. All
776 experiments were conducted under IACUC-approved protocols and complied with the Animal
777 Welfare Act and the National Institutes of Health guidelines for the ethical care and use of animals
778 in biomedical research.

779

780 *Cell lines*

781 Cell lines used in these studies included MC38, a murine colon tumor model on the B6
782 background; NThyOri-3.1, a human thyroid follicular cell line generated by SV40 transformation
783 of normal thyroid cells; 293 T cells, a human embryonic kidney cell line; and CHO-mTPO, Chinese
784 hamster ovary cells stably transfected for surface membrane expression of mouse thyroid
785 peroxidase (TPO) protein expression⁶⁷. Tumor cell lines were obtained from the American Type
786 Culture Collection [(ATCC), MC38 and NThyOri-3.1] or were gifted to Dr. Lechner or Dr. Su
787 (CHO-mTPO cells by Drs. Basil Rapoport and Sandra McLachlan; 293T cells by Dr. Christopher
788 Seet; MC38 cells by Dr. Antoni Ribas). Tumor cell line authenticity was performed by surface
789 marker analysis performed at ATCC or in our laboratory. MC38, NThyOri-3.1 and 293T cells were
790 grown in complete medium [RPMI-1640 supplemented with 10% fetal bovine serum (FBS), 2mM
791 L-glutamine, 1mM HEPES, non-essential amino acids, and antibiotics (100 U/mL Penicillin and
792 100 µg/mL Streptomycin)], at 37°C in humidified, 5% CO₂ incubators. CHO-mTPO cells were
793 cultured in F12 media supplemented with 10% FBS, 2mM L-glutamine, 1mM HEPES, non-

794 essential amino acids, and antibiotics (100 U/mL Penicillin and 100 µg/mL Streptomycin). Cell
795 lines were monitored regularly for phenotype. Early passage cells were used for experiments (P1
796 or P2).

797

798 *Reagents and media*

799 Immune checkpoint inhibitor antibodies used were anti-mouse PD1 (clone RPM1-14), CTLA-4
800 (clone 9D9), and isotype controls [clone 2A3 and MPC-11, respectively] (BioXcell). For inhibitor
801 experiments, a neutralizing antibody against mouse interleukin-17A (clone 17F3) and mouse
802 tumor necrosis factor α (clone XT3.11), from BioXCell. Antibodies were diluted in sterile PBS for
803 use. Human recombinant cytokines IL-17A and TNF α from PeproTech and R&D Systems,
804 respectively, were reconstituted and stored per manufacturer instructions. For *in vitro*
805 experiments, primary immune cells were cultured in RPMI complete media [supplemented with
806 10% fetal bovine serum (FBS), 2mM L-glutamine, 1mM HEPES, non-essential amino acids, and
807 antibiotics (penicillin and streptomycin)], with 50uM beta-mercaptoethanol.

808

809 *Immune checkpoint inhibitor treatment of mice*

810 Groups of 4-6 week old NOD or B6 mice were used for ICI inhibitor experiments. Mice were
811 randomized to twice weekly treatment with anti-mouse CTLA-4 (clone 9D9), or PD-1 (RPM1-14),
812 both anti-CTLA-4 and anti-PD-1, or an isotype control (2A3, MPC-11), at 10 mg/kg/dose
813 intraperitoneally (*i.p.*) for four or eight weeks. During treatment mice were monitored daily for
814 activity (including signs of neuropathy) and appearance, and twice weekly for weight and
815 glucosuria. Mice developing glucosuria were treated with 10 units of subcutaneous NPH insulin
816 daily. Thyroid dysfunction was assessed by measurement of free thyroxine (FT4) in sera by ELISA
817 (LSBio). After four or eight weeks of ICI treatment (as indicated), mice were euthanized, blood
818 collected by retro-orbital bleed, then perfused with 10mL of phosphate buffered saline (PBS).
819 Tissues were collected for histologic analysis into neutral buffered formalin, including thyroid,

820 lacrimal and salivary glands, lung, liver, kidney, heart, colon, eye, gonad, and pancreas. Serum
821 was collected from blood (centrifugation 1000xg for 30 min). Predetermined endpoints for
822 euthanasia before four weeks included >20% weight loss and glucosuria not resolved by insulin
823 therapy, as per IACUC protocols.

824

825 *Histology*

826 Harvested organs were fixed in 10% buffered formalin for at least 96 hours and then stored in
827 70% ethanol. Organs were embedded in paraffin, sectioned (4 μ m), and stained with hematoxylin
828 and eosin (H&E) by the UCLA Translational Pathology Core Laboratory. Immune infiltration was
829 assessed on H&E sections using an adapted immune infiltrate scoring system reported
830 previously³⁵. The presence of interstitial inflammation, lymphocytic aggregates, perivascular
831 inflammation, follicular disruption, and Hurthle cell change was assessed as either present or
832 absent on H&E tissue sections by a clinical pathologist (E.D.R.). In addition, each tissue was
833 given an aggregate immune infiltrate score of 0 (no immune infiltrate), 1 (1-2 focal areas of
834 immune infiltrate and/or sparse interstitial inflammation), 2 [>2 focal areas of immune infiltration,
835 and/or presence of both focal glomerulonephritis and perivascular immune infiltration (kidney),
836 and/or diffuse immune infiltrate affecting $>25-49\%$ of the tissue area] or 3 (diffuse immune infiltrate
837 affecting $>50\%$ of the tissue area). For pancreas tissue, immune infiltrate score was modified as
838 0 for no immune infiltrate, 1 for $<50\%$ of islets affected by immune infiltration, or 2 for $>50-100\%$
839 of islets affected by immune infiltration. The enumeration and typing of inflammatory infiltrate were
840 assessed through immunohistochemical stains (see below). Immune scoring was done by two
841 blinded individuals evaluating at least 10 high powered fields per section for pancreas, lung, liver,
842 heart, thyroid, kidney, salivary, gut (colon and stomach), and gonad tissues; for small tissues
843 (lacrimal glands and eye) 5 high powered fields were evaluated. Images were acquired on an
844 Olympus BX50 microscope using Olympus CellScans Standard software. Images were
845 brightened uniformly for publication in Photoshop.

846

847 *Immunohistochemistry*

848 For immunohistochemistry (IHC), 4mm FFPE tissue sections were deparaffinized, rehydrated,
849 and subjected to heat-induced antigen retrieval (0.01 mol/L citrate, pH 6.0) followed by treatment
850 with 3% H₂O₂ for 10 minutes to block endogenous peroxidase activity. Sections were incubated
851 overnight at 4°C with primary antibodies against mouse IL17A (Abcam, ab91649, 1:50 dil), CD3
852 (DAKO, clone A0542, 1:100 dil), F4/80 (BioRad, clone MAC497G, 1:200 dil), B220 (BD, clone
853 RA3-6B2, 1:50 dil), IL-17RC (Bioss, catalog BS-2607R, polyclonal, 1:300 dil). Sections were then
854 stained with appropriate secondary antibodies and antigen detection done with 3,3'-
855 diaminobenzidine. Sections were counterstained with hematoxylin, dehydrated, and mounted.
856 Appropriate positive and negative controls were used for all stains. Brightness of all images was
857 increased by 50 in Adobe Photoshop. Positively stained leukocytes for CD3, B220, F4/80, or IL-
858 17A were counted in 10 representative high-power fields (hpf, total 400x magnification) for each
859 tissue section. Two independent observers scored each section and the results were pooled with
860 rare disagreements resolved by a third evaluator.

861

862 *ELISA for thyroglobulin antibody*

863 Mouse anti-thyroglobulin antibodies were measured via ELISA as previously reported²⁷. Briefly,
864 96-well plates were coated with 50uL of 1.5mg/mL purified mouse thyroglobulin (mTg, generously
865 provided by the Rapoport lab) in Coating Buffer (30mM Na₂CO₃, 70mM NaHCO₃, 6mM NaN₃,
866 pH 9.3) covered and incubated at 4°C overnight. The following day, plates were washed twice
867 with 100uL per well Tris/NaCl (200mM Tris base, 188mM NaCl, pH 7.4), once with Tris/NaCl
868 Tween (Tris/NaCl, 500uL/L Tween 20), and once more with Tris/NaCl. Plates were blocked with
869 100uL/well Blocking Buffer (5% w/v BSA, 150mM NaCl) for twenty minutes at room temperature
870 (RT) then washed again as above. Sera samples were diluted 1:100 in PBS and added to wells
871 in triplicate. Plates were covered and allowed to incubate RT 1.5 hours. Plates were washed four

872 times with 100uL/well of Tris/NaCl Tween. Anti-mouse IgG1-HRP was diluted 1:2000 in
873 Secondary Antibody Buffer (1% w/v BSA, 150mM NaCl) and was added to plate at 100uL/well.
874 Plate was covered and allowed to incubate RT one hour, then washed four times with 100uL/well
875 Tris/NaCl Tween. ELISA was read by adding 100uL/well TMB substrate (Thermo Scientific,
876 N301), allowing 10 minutes to develop in dark, and read on a spectrophotometer at OD 605nm.

877

878 *Thyroid peroxidase antibody*

879 Mouse thyroid peroxidase antibody (TPO) antibody levels were detected using mouse sera
880 binding on CHO-mTPO cells, followed by flow cytometry as previously described²⁷. Briefly,
881 experimental mouse sera were incubated with a single cell suspension of mouse CHO-mTPO
882 cells at a 1:50 dilution in Buffer A (2% FBS in PBS with 10mM HEPES) for 45 minutes at 4°C,
883 then washed twice with Buffer A. For detection of immunoglobulin binding, samples were then
884 incubated with goat anti-mouse IgG FITC secondary antibody at 10ug/mL for 30 minutes at 4°C
885 and then washed twice with Buffer A. Finally, mean fluorescence intensity of FITC was measured
886 for live, single CHO-cells using an Attune NxT 6 cytometer (ThermoFisher).

887

888 *Flow Cytometry*

889 Immediately after euthanasia and perfusion with sterile PBS, fresh tissues were dissociated for
890 analysis of immune infiltrates by flow cytometry. Thyroid glands were dissected away from
891 surrounding trachea and lymphoid tissue, digested in collagenase IV (1mg/mL in 2% FBS in PBS)
892 at 37°C for 20 minutes, then mechanically dissociated by passage through a 40um filter. Spleen
893 cells were isolated by mechanical dissociation and passage through a 40um filter. To assess
894 intracellular cytokines, cells were incubated in complete RPMI media with 50uM 2ME for four
895 hours with ionomycin (1ug/mL) and PMA (50ng/mL) in the presence of Brefeldin A prior to
896 staining. For staining, single cell suspensions were resuspended in FACS buffer (0.5mM EDTA,
897 2% FBS in PBS) at 10⁶cells/mL and stained with fluorescence conjugated antibodies. For

898 intracellular staining, after surface staining, cells were fixed and permeabilized using cytoplasmic
899 fixation and permeabilization kit (BD, for cytokines IL-17A and IFN γ) or FoxP3 transcription factor
900 kit (eBioscience, for ROR γ t), per protocol instructions, with 30 min fixation at 4°C. Viability dye
901 DAPI was added prior to analysis where indicated. Cells were then washed twice in FACS buffer
902 and analyzed by flow cytometry on an Attune NxT 6 cytometer (ThermoFisher). Antibodies used
903 are shown in **Supplemental Methods**. Cell counts are shown as relative frequency of live, gated
904 single cells unless otherwise noted. For determination of infiltrating cells per thyroid lobe, whole
905 perfused thyroid specimens were dissociated to single cell suspensions and the entire specimen
906 stained for flow cytometry and a fixed volume of the specimen was evaluated by flow cytometry
907 to allow back calculation for estimate of absolute cell count (e.g. 100ul of 200ul total sample
908 volume run yields a 2x multiplier for cell count).

909

910 *Neutralizing antibody studies in ICI-treated mice*

911 Groups of 4-6 wk old NOD mice were randomized to treatment with anti-mouse PD-1 (clone
912 RPM1-14) plus anti-mouse CTLA-4 (9D9) antibodies or isotype controls (2A3 plus MPC-11) at
913 10mg/kg/dose twice weekly by *i.p.* injection. Additionally, 10 days after start of ICI or isotype
914 therapy, mice were further randomized to receive neutralizing antibody to IL-17A (clone 17F3),
915 TNFa (clone XT3.11), combination or vehicle alone (PBS).

916

917 *Tumor model studies*

918 Groups of 6-week old C57/B6 mice were inoculated s.c. with 3×10^5 MC38 tumor cells in the flank,
919 as described previously⁷⁴, and randomized into groups ($n=6$) for treatment when tumor volumes
920 reached 40–80mm³. Groups of mice received no treatment (PBS vehicle only), combination ICI
921 [anti-PD-1 (clone RPM1-14) + anti-CTLA-4 (clone 9D9) at 10mg/kg/dose], or combination ICI with
922 a neutralizing antibody to mouse IL-17A (clone 173F, 0.5mg/dose) or isotype control (catalog

923 BE0088). Reagents were given by *i.p.* injection on the ipsilateral side to the tumor. Mouse tumor
924 volumes were measured every 2 days by caliper and mice were sacrificed when tumor volumes
925 reached 2cm in diameter or when animal morbidity mandated sacrifice under institutional vivarium
926 protocols.

927

928 *Stimulation of human thyroid cell line NThy-Ori-3.1*

929 To determine the effects on antigen presentation and cytokine production of IL-17A and TNF α on
930 the human thyroid cell line NThy-Ori 3.1, an *in vitro* test of cytokine exposure was used to evaluate
931 RNA for gene expression changes. The 1.0×10^5 Thy Ori 3.1 cells were plated in 1 mL of 10%
932 RPMI in a 24-well plate. Once the cells were adherent, 50 ng/mL of each cytokine or vehicle (PBS,
933 IL-17A, TNF α , or IL-17A+TNF α) was added per well and were allowed to incubate at 37°C. Each
934 condition had four biological replicates. After the eight hour stimulation, cells were used for RNA
935 extraction and quantitative reverse transcriptase PCR.

936

937 *Quantitative reverse transcriptase PCR (qRT-PCR)*

938 For RNA extraction, human NThy-Ori-3.1 cells were washed twice with PBS, then lysed directly
939 in tissue culture wells. For mice experiments, resected mouse thyroid lobes were snap frozen in
940 liquid nitrogen and stored at -80°C. Multiple thyroid lobes were homogenized in RNA Lysis Buffer
941 (Zymo Research) using the Fisherbrand 150 Handheld Homogenizer (15-340-167). RNA
942 extractions were performed using Quick-RNA Microprep kit (Zymo Research, R1051) per
943 manufacturer's instructions. RNA yield was quantified by nanodrop. RNA was converted into
944 cDNA using High-Capacity cDNA Reverse Transcription Kit with RNase Inhibitor and MultiScribe
945 Reverse Transcriptase (Applied Biosystems, 4374966) following manufacturer's instructions.
946 About 750 ng/uL of RNA was used for cDNA synthesis per reaction. Quantitative PCR was
947 performed using Taqman Fast Advanced PCR Master Mix (Applied Biosystems, 4444557) and
948 Taqman probes for genes of interest (**Supplemental Methods**), with three technical replicates

949 per gene, per condition. PCR cycles were run using the QuantStudio 6 Pro PCR machine (Applied
950 Biosystems) with the standard cycle parameters. Design and Analysis QuantStudio 6/7 Pro
951 Systems Software (Thermo Fisher Scientific, Version 2.5.0) was used to identify amplification of
952 genes and calculate fold change from Cq values. In this context, fold change was the expression
953 ratio of the gene of interest to the housekeeping gene, GAPDH. For further analysis of NThy-Ori-
954 3.1 antigen presentation and cytokine production, human 293T cells were also used for qRT-PCR
955 to compare upregulated gene expression.

956

957 *Patients*

958 Patients were prospectively enrolled from two academic medical centers (UCLA Health, USC
959 Keck Medical Center) under IRB approved protocols (19-000032, 19-001708, HS-19-00715).
960 Peripheral blood specimens were collected from adult (age >18 years) patients under several
961 categories: ICI-treated cancer patients ($n=20$, including 18 with thyroid or other IrAE or no IrAE),
962 Hashimoto's thyroiditis (HT, $n=13$), or healthy control ($n=6$) with no evidence of thyroid disease.
963 Exclusion criteria included pregnancy, history of thyroid surgery, radioactive iodine therapy, or
964 thyroid cancer, immune modifying conditions not including solid malignancy (e.g. bone marrow
965 transplantation, leukemia or lymphoma, known genetic or acquired immunodeficiency, or immune
966 modifying medications at the time of specimen collection, excluding physiologic steroids). ICI-
967 treated subjects must have received an FDA-approved ICI within the past 1 month. ICI treatment
968 included combination anti-CTLA-4 + anti-PD-1 in 5 subjects, single agent anti-PD-1/L1 in 8, and
969 sequential in 7 (anti-CTLA-4 + anti-PD1, then anti-PD-1 in 6 subjects and anti-PD-1, followed by
970 combination in 1 subject). Cancer types were as follows: melanoma ($n=9$), renal cell ($n=5$), breast
971 ($n=2$), lung squamous cell ($n=1$), sarcoma ($n=1$), neuroendocrine ($n=1$) hepatocellular ($n=1$). HT
972 patients had hypothyroidism (elevated TSH and low FT4, and/or requirement for thyroid hormone
973 replacement) and evidence of thyroid autoimmunity (e.g. thyroid auto-antibody presence: anti-
974 TPO or anti-Tg); imaging findings if available were consistent with HT. Controls without thyroid

975 disease included subjects with normal thyroid hormone status (TSH and FT4), absence of anti-
976 TPO and anti-Tg antibodies, and no history of thyroid disease; subjects may have a benign
977 nodule. Peripheral blood mononuclear cells were isolated from blood by density gradient
978 centrifugation (Ficoll).

979

980 ***Single cell RNA sequencing***

981 For mouse scRNAseq studies, CD45⁺ infiltrating cells were isolated from fresh thyroid tissue. To
982 reduce contamination from circulating immune cells in the blood, animals were perfused with
983 normal saline prior to tissue collection. Thyroid tissue was enzymatically and mechanically
984 dissociated, then single cell suspensions stained with fluorescence-conjugated antibodies to
985 CD45, CD11b, CD3, CD4, CD8, and CD19 and viability dye DAPI. Specimens with and potential
986 cervical LN or thymus contamination were excluded by detection of >20% double positive CD4⁺
987 CD8⁺ T cells⁷⁵. 10,000 cells were submitted for 10x single cell transcriptomic sequencing. Library
988 construction and sequencing was done by the UCLA Technology Center for Genomics and
989 Bioinformatics (TCGB) core facility.

990

991 *Data processing of scRNA-seq libraries*

992 After sequencing, the scRNA-seq reads were aligned to the mm10 (mouse) reference genome
993 and quantified using the 10x Genomics cellranger count software. Filtered output matrices that
994 contained only barcodes with unique molecular identifier (UMI) counts that passed the threshold
995 for cell detection were used for downstream analysis.

996

997 *Normalization, Principal Component analysis, and UMAP Clustering*

998 Downstream analysis was done with Seurat v3⁴⁵. Only cells with a mitochondrial gene percentage
999 less than 30% and 200 features were included in downstream analysis. Scores for S and G2/M
1000 cell cycle phases were assigned using the Seurat CellCycleScoring function following the

1001 standard Seurat pipeline⁷⁶. UMI counts were log normalized, and the top 2000 variable genes
1002 were determined using the variance-stabilizing transformation (vst) method. All genes were
1003 scaled and centered using the ScaleData function, and principal component analysis (PCA) was
1004 run for the data using the predetermined variable genes. To group cells into clusters, a K-nearest
1005 neighbors graph function (implemented in the Seurat package), followed by a modularity-
1006 optimizing function using the Louvain algorithm was used. For the cluster, 30 PC dimensions were
1007 included and the resolution parameter was set to 0.4. Cell-type clusters were visualized using
1008 uniform manifold approximation and projection (UMAP) to reduce dimensionality and allow for the
1009 cells to be visualized on a 2-D plot.

1010

1011 *Differential Expression and Marker Gene Identification*

1012 The Seurat findMarkers function was used to generate the top upregulated genes for each cluster
1013 using a Wilcoxon Rank Sum Test to identify differentially expressed genes across clusters. Marker
1014 genes were filtered by a minimum of detectable expression in 25% of the cells in the target group
1015 and minimum log2 fold change of 0.25. The markers generated by these functions were compared
1016 to markers for known cell types to assign identities to the different clusters. Differentially
1017 expressed genes across conditions were identified using the same function and parameters.

1018

1019 *Integration and Subsetting of Datasets*

1020 For analysis of different immune cell subsets (T cell, Rorc⁺ and B/myeloid cells), variable features
1021 were recomputed for each subset and downstream analyses including scaling, PCA, and UMAP
1022 were rerun. Initial cell clustering for CD45⁺ immune cells identified a cluster of likely cervical
1023 thymus contamination origin (double positive *Cd4* and *Cd8a*-expressing cells by correlation
1024 analysis, with co-expression of *Cd24a*, *Rag2*, *Rag1*, and *Dnrtt*) as previously reported in mouse
1025 neck tissue⁷⁵. To remove potential thymic contamination from subsequent *Cd3* and *Rorc*
1026 subclustering, cells expressing *Rag1* at an expression level greater than 1 were removed. For

1027 *Cd3* subclustering, *Cd3*⁺ subsets were manually selected from CD45⁺ UMAP and reclustered.
1028 Similarly, B cell, myeloid and APC subclustering from mouse CD45⁺ cells was done similarly. For
1029 the *Rorc*⁺ subclustering in mouse dataset, all cells from the T-cell subset expressing *Rorc* at an
1030 expression level greater than 1 were selected for analysis.

1031
1032 We used the CellChat R package (version 0.5.5) to makes inferences about potential cell-cell
1033 interactions using the gene expression of murine receptors and ligands in the CellChatDB, a
1034 database curated by Jin *et al.*⁷⁷ containing genes from peer-reviewed literature and the Kyoto
1035 Encyclopedia of Genes and Genomes (KEGG). CellChat performs a comprehensive analysis of
1036 signaling gene expression; its database considers multiple complexes' subunits, which must all
1037 be expressed for a signaling pathway to be considered significant. The same requirements were
1038 also applied on cofactors and mediators of cell communication. These curated signaling genes
1039 are grouped into biologically relevant pathways such as CXCL and CCL (genes comprising each
1040 pathway shown in **Extended Data Table 2**).

1041
1042 Transcriptomic data from thyroid-infiltrating Cd45⁺ immune cells from ICI-treated mice were
1043 imported from the Seurat analysis pipeline which allowed CellChat to make use of the manually
1044 assigned cluster labels. Our analysis closely followed the example created by Jin *et al.*⁷⁷
1045 (<https://github.com/sqjin/CellChat>). CellChat requires the data to be sub-sampled using geometric
1046 sketching to reduce the computational workload using the `subsetData` function⁷⁸. Comparison of
1047 expression of genes from CellChatDB across cell clusters was performed with the
1048 `identifyOverExpressedGenes` and `identifyOverExpressedInteractions` functions using a Wilcoxon
1049 rank sum test using the default significance level of 0.05. Communication probability (or strength
1050 of interaction) was calculated using an equation described in Jin *et al.*⁷⁷ based on the law of mass
1051 action using the function `computeCommunProb`. Average gene expression was calculated using
1052 the default trimean approach. Signaling pathways were determined to be significantly expressed

1053 using a permutation test using the default number of permutations ($M = 100$) and default
1054 significance threshold (p -value < 0.05). Signaling pathways were filtered to remove those
1055 expressed in fewer than 10 cells in a single cluster using the filterCommunication function.
1056 Signaling probabilities for each pathway were generated by analyzing the average expression of
1057 each pathway's receptors and ligands computed by earlier analysis using the
1058 computeCommunProbPathway function. The source, recipient, and mediating cell groups were
1059 determined by analyzing the average pathway expression by each cell cluster using the
1060 aggregateNet function and the netAnalysis_computeCentrality function. These analyses were
1061 visualized using CellChat's circle and hierarchy plot and heatmap functions.

1062

1063 *Statistics*

1064 Data were analyzed with GraphPad Prism v9. Descriptive statistics shown are mean + SEM for
1065 continuous variables. Differences in the mean frequency of immune cells or gene expression for
1066 qRT-PCR between two groups were evaluated by two-sided t test with Welch correction for
1067 potential differences in variance among groups and correction for multiple comparisons by the
1068 Holm-Sidak method. For B6 mice, differences in organ immune infiltrate score, thyroid
1069 autoantibodies (TPO MFI and Tg ELISA OD) were compared between groups by two-tailed,
1070 unpaired t test with Welch correction, without assumption of equal s.d. Differences in the mean
1071 frequency of immune cells, organ immune infiltrate score, thyroid autoantibodies (TPO MFI and
1072 Tg ELISA OD) among groups were evaluated by Brown-Forsythe ANOVA with Welch correction
1073 for potential differences in variance among groups, followed by multiple comparisons between
1074 groups with Dunnett correction for multiple comparisons (two-tailed comparisons). Where
1075 appropriate, adjusted p values are shown. Significance was set at an alpha = 0.05. Samples sizes
1076 for each group or condition are shown.

1077

1078 *Data availability*

1079 Data associated with figures are available from the corresponding author upon reasonable
1080 request. The datasets for single cell sequencing generated during and analyzed during the current
1081 study will be available in the GEO repository (<https://www.ncbi.nlm.nih.gov/geo/>).

1082

1083 **Methods References**

- 1084 74. Moreno, B. H. *et al.* Response to programmed cell death-1 blockade in a murine
1085 melanoma syngeneic model requires costimulation, CD4, and CD8 T cells. *Cancer*
1086 *Immunol. Res.* **4**, 845–857 (2016).
- 1087 75. Terszowski, G. *et al.* Evidence for a functional second thymus in mice. *Science* **312**, 284–
1088 287 (2006).
- 1089 76. Tirosh, I. *et al.* Dissecting the multicellular ecosystem of metastatic melanoma by single-
1090 cell RNA-seq. *Science* (80-.). **352**, 189–196 (2016).
- 1091 77. Jin, S. *et al.* Inference and analysis of cell-cell communication using CellChat. *bioRxiv* 1–
1092 20 (2020) doi:10.1101/2020.07.21.214387.
- 1093 78. Hie, B., Cho, H., DeMeo, B., Bryson, B. & Berger, B. Geometric Sketching Compactly
1094 Summarizes the Single-Cell Transcriptomic Landscape. *Cell Syst.* **8**, 483-493.e7 (2019).

1095

1096 **Acknowledgements**

1097 This work was supported by funding from the American Thyroid Association
1098 (THYROIDGRANT2020-0000000169, M.G.L.), UCLA Specialty Training and Advanced Research
1099 (STAR) program (M.G.L.), Parker Institute for Cancer Immunotherapy (M.A.S.), and UCLA core
1100 facilities [Broad Stem Cell Research Center FACS core, Translational pathology core laboratory
1101 (TPCL), and Technology Center for Genomics and Bioinformatics (TCGB)]. The authors would
1102 like to acknowledge Drs. Sandra McLachlan and Basil Rapoport for CHO-mTPO cell line and
1103 methods for thyroid autoantibody detection.

1104

1105 **Author contributions**

1106 M.G.L., W.H., T.E.A., A.D., and M.A.S. conceived the study and designed the analysis.
1107 M.G.L., A.Y.P., T.E.A., M.S.P., N.Y., M.I.C., A.T.H., and L.G. collected the data, including
1108 mouse experiments with ICI treatment, patient specimens, flow cytometry, qRT-PCR,
1109 immunohistochemistry, and tumor model studies. W.H., A.R., A.D., H.C., and M.A. S.
1110 contributed data and analysis tools. M.G.L., A.Y.P., M.S.P., N.Y., A.T.H., E.C.M., E.D.R.,
1111 and H.C. performed the analysis. M.G.L., A.Y.P., W.H., T.E.A., M.A.S., A.T.H., H.C., N.Y.,
1112 E.C.M., A.D., A.R., and M.A.S. wrote or edited the paper. All authors reviewed the
1113 manuscript.

1114

1115 **Competing interests**

1116 A.R. has received honoraria from consulting with Amgen, Bristol-Myers Squibb, Chugai,
1117 Genentech, Merck, Novartis, Roche, Sanofi and Vedanta, is or has been a member of the
1118 scientific advisory board and holds stock in Advaxis, Appia, Apricity, Arcus, Compugen, CytomX,
1119 Highlight, ImaginAb, Isoplexis, Kalthera, Kite-Gilead, Merus, PACT Pharma, Pluto, RAPT,
1120 Rgenix, SyntheKine and Tango, has received research funding from Agilent and from Bristol-
1121 Myers Squibb through Stand Up to Cancer (SU2C), and patent royalties from Arsenal Bio. All
1122 other authors have declared no conflicts of interest.

1123

1124 **Additional information**

1125 Extended data is available for this paper.

1126 Supplementary information is available for this paper.

1127 Correspondence and materials requests should be directed to Dr. Melissa Lechner, Division of
1128 Endocrinology, Diabetes, and Metabolism, UCLA, 10833 Le Conte Ave, CHS 57-145, Los
1129 Angeles, CA, 90095. Email: MLechner@mednet.ucla.edu; Phone: 310-794-3237.

1130

1131

1132 **Extended Data Tables**

1133 Extended Data Table 1. Top gene lists for scRNAseq data.

1134 Extended Data Table 2. Ligand-Receptor interaction pathway genes in CellChat analyses.

1135

1136 **Extended Data Figure Legends**

1137 **Extended Data Fig. 1. Flow cytometry analysis of thyroid-infiltrating immune cells in anti-**

1138 **PD-1 + anti-CTLA-4 (Dual ICI) treated B6 mice.** Mice were euthanized after 4 weeks of ICI or

1139 isotype treatment, perfused with saline, and then fresh thyroid tissues dissociated into single cell

1140 suspensions. Cells were stained with fluorescent antibodies and analyzed by flow cytometry, with

1141 estimation of cells/thyroid lobe for each animal. Each point represents an individual mouse ($n=8$

1142 isotype and $n=8$ Dual ICI). Mean frequencies of cell populations shown between groups were

1143 compared by two-tailed, unpaired t test with Welch correction, assuming unequal s.d., and Holm-

1144 Sidak method correction for multiple comparisons, with $p<0.05$ considered significant. The p

1145 values for all comparisons were not significant.

1146

1147 **Extended Data Fig. 2. Additional histologic data for immune infiltrates in ICI-treated NOD**

1148 **mice.** Representative H&E micrographs showing autoimmune tissue infiltrates in Dual ICI vs.

1149 isotype treated mice (original mag. 100x-400x). Shown are isotype treated mice tissues (*left*) and

1150 Dual ICI-treated mice tissues (*right*) for organs noted to have infiltrates in multiple animals. Arrows

1151 indicate areas of autoimmune infiltration.

1152

1153 **Extended Data Fig. 3. Flow cytometry analysis of peripheral immune changes in ICI-treated**

1154 **NOD mice.** Frequency of putative natural killer (NK, NKp46⁺ CD3⁻), NKT (CD3⁺ NKp46⁺), B

1155 (B220⁺ CD3⁻ NKp46⁻ CD11b⁻), myeloid (CD11b⁺) and conventional dendritic cell (DC, CD11c⁺

1156 CD11b^{low}) as a percent of splenocytes in isotype ($n=7$) vs. anti-PD-1 + anti-CTLA-4 (Dual ICI,
1157 $n=8$) mice after 4 weeks of treatment. Differences in immune populations in spleen were
1158 compared by two-tailed, unpaired t test with Welch correction, assuming unequal s.d., and Holm-
1159 Sidak method correction for multiple comparisons. The adjusted p values are as follows: NK cell
1160 0.004, NKT cell 0.002, B cell 0.12, CD11b⁺ myeloid cell 0.3, and DC 0.16.

1161

1162 **Extended Data Fig. 4. Additional scRNAseq analysis of thyroid infiltrating immune cells**
1163 **from ICI-treated NOD mice.**

1164 a, Heatmap showing top 10 variable genes expressed in cell clusters for CD45⁺ thyroid-infiltrating
1165 immune cells from ICI-treated NOD mice. b, Feature plots showing expression of immune cell
1166 population-associated genes CD45⁺ thyroid-infiltrating immune cells. c, Heatmap showing top 10
1167 variable genes expressed in cell clusters for sub-clustered *Cd3*⁺ cells. d, Violin plots for type 1
1168 immunity (top left, *Tbx21*, *Ifng*), T cell activation (bottom left, *Cd69* and *Cd44*), and cytotoxicity-
1169 associated (right, *Prf1*, *Gzmk*, *Fasl*, and *Nkg7*) genes in cell clusters for sub-clustered *Cd3*⁺ cells.
1170 e, Heatmap showing top 20 variable genes expressed in cell clusters for sub clustered *Rorc*⁺ cells.

1171

1172 **Extended Data Fig. 5. Pro-inflammatory myeloid populations in thyroid immune infiltrates**
1173 **of ICI-treated mice.**

1174 a, Subcluster of myeloid and B cells from CD45⁺ thyroid infiltrating cells in ICI-treated mice. UMAP
1175 shows 7 distinct clusters. b, Heatmap of top 10 genes in subclustered cells. c, Feature and violin
1176 plots for expression of inflammatory cytokines including *Tnf*, *Il1b*, and *Tgfb1*. d, Intrathyroidal gene
1177 expression in ICI-treated vs. isotype mice measured by qRT-PCR ($n=12$ animals group for all
1178 genes except $n=4$ for *Il1b*; thyroid tissue pooled and run in 3 experiments; qRT-PCR reactions in
1179 triplicate). Relative gene expression shown as mean fold change \pm SEM for ICI-treated fold
1180 change over isotype. Comparison by two-tailed, unpaired t test with Welch correction, assuming
1181 unequal s.d., and Holm-Sidak method correction for multiple comparisons. Adjusted P values are

1182 <0.0001 for *Tnf*, *Il6*, and *Tgfb1*; one pooled sample evaluated for *Il1b* so statistical significance
1183 was not tested. *e*, Macrophage and dendritic cell clusters showed likely signaling interactions via
1184 CXCL pathways to effector CD4 and CD8, $\gamma\delta$ T, and NK/NKT cells, as predicted by ligand-receptor
1185 interactions in transcriptomic data using CellChat.

1186

1187 **Extended Data Fig. 6. Potential action of IL-17A on thyroid epithelial cells.**

1188 *a*, IHC staining for IL-17 receptor C (IL-17RC) in thyroid tissue of Dual ICI-treated mice (*top left*).
1189 Murine stomach tissue stained for IL-17RC positive control (*bottom left*) and secondary only
1190 controls (*right*) shown for comparison (representative sections, original mag. 400x). *b*, Relative
1191 gene expression of IL-17RC (*Il17rc*) measured by qRT-PCR in human NThyOri-3.1 cells treated
1192 with vehicle alone ($n=3$), recombinant human IL-17A ($n=3$), TNF α ($n=3$), or both ($n=3$) for 8 hours.
1193 Gene expression normalized to housekeeping gene and shown relative to human 293T cells
1194 ($n=4$). Comparison of NThy-Ori-3.1 to 293T cells by two-tailed, unpaired t test with Welch
1195 correction, assuming unequal s.d., with p value of 0.04.

1196

1197 **Extended Data Fig. 7. Gating strategy and representative dot plot for human peripheral**
1198 **blood mononuclear cell staining for T cell populations and interleukin (IL)-17A.**

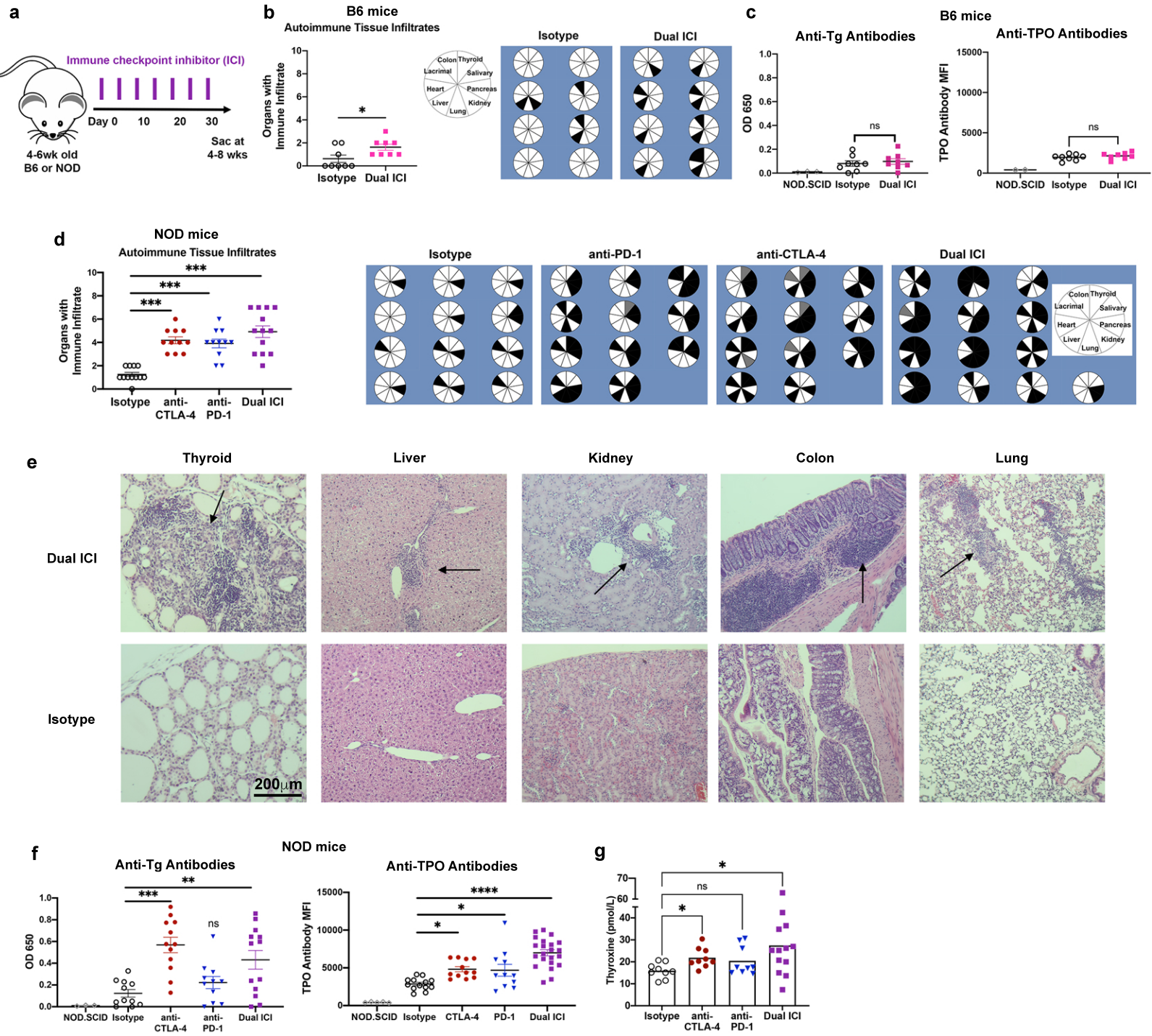


Figure 1. ICI therapy induces multi-system autoimmune infiltrates (IrAE) in B6 and NOD mice.

a, Schematic of ICI drug treatment. **b**, Comparison of autoimmune organ infiltration after 4 weeks of ICI vs. isotype treatment in C57/B6 (B6) mice ($n=8$ isotype, $n=8$ Dual ICI); Pie charts (right) show tissue infiltrate for each mouse; black = immune infiltrate, white = no infiltrate, gray = no data. **c**, Quantification of anti-thyroid autoantibodies in B6 mice after 4 weeks of isotype ($n=8$) or Dual ICI ($n=8$) treatment. **d**, Comparison of autoimmune organ infiltration after 8 weeks of ICI treatment in NOD mice ($n=12$ isotype, $n=11$ anti-CTLA-4, $n=11$ anti-PD-1, and $n=13$ Dual ICI). Pie charts show tissue infiltrate for each mouse, as in **b** above. **e**, Representative H&E micrographs of autoimmune tissue infiltrates in Dual ICI vs. isotype treated mice (original mag. 100x). **f**, Quantification of anti-thyroid autoantibodies in NOD mice after 8 weeks of treatment ($n=10$ isotype anti-Tg or 13 for anti-TPO, $n=12$ anti-CTLA-4, $n=11$ anti-PD-1, and $n=13$ Dual ICI for anti-Tg or 22 for anti-TPO). **g**, Free thyroxine serum levels in ICI-treated NOD mice after 8 weeks of treatment. Data are mean \pm SEM. * $p<0.05$, ** $p<0.01$, *** $p<0.001$, unpaired t test, two-tailed (**b,c**), Brown-Forsythe ANOVA, assuming unequal s.d., followed by Dunnett's multiple comparisons test (**d,g**), or one-way ANOVA and Dunnett's multiple comparison test (**f**).

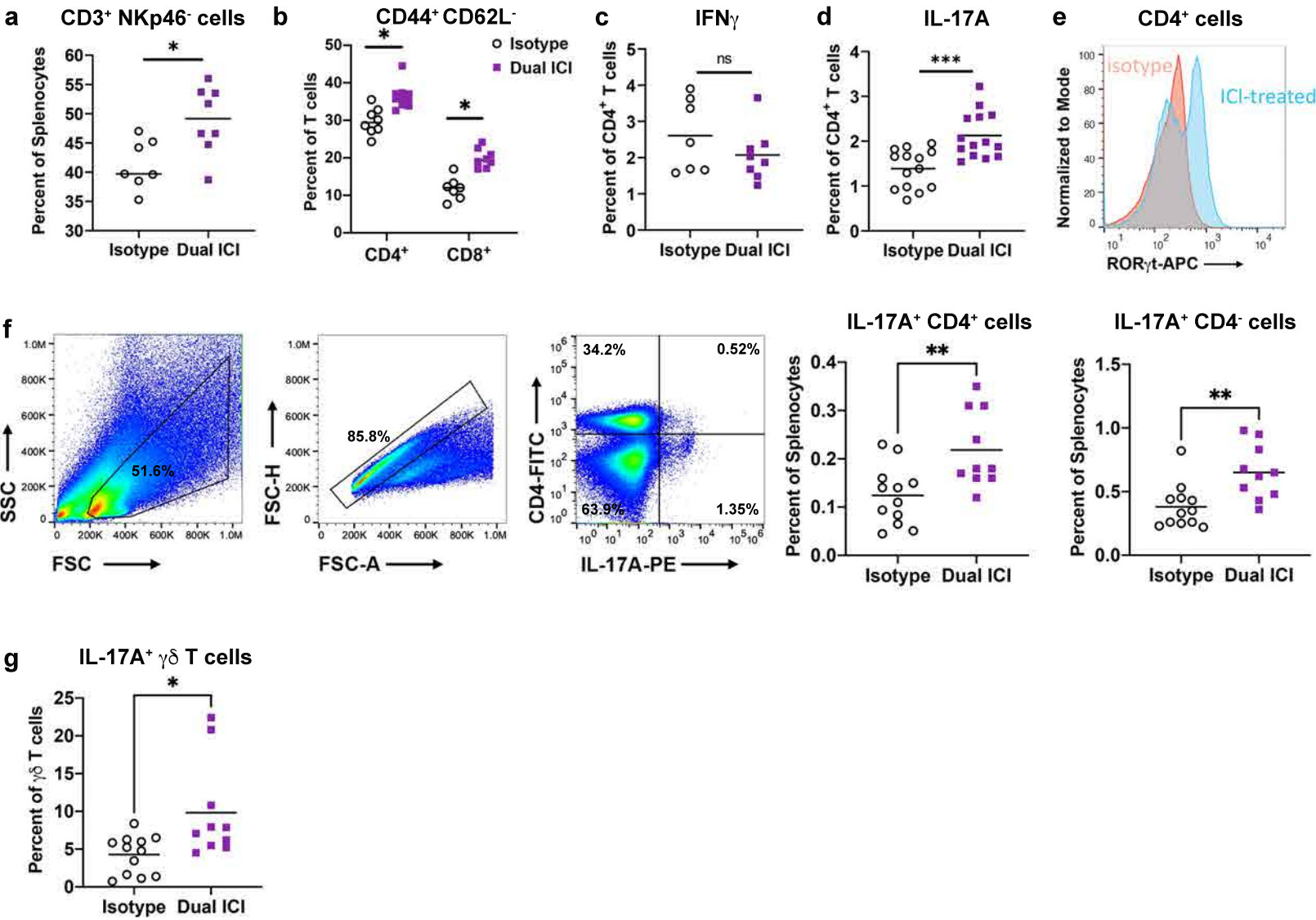


Figure 2. Flow cytometry analysis of peripheral immune changes in ICI-treated NOD mice.

a, Frequency of CD3⁺ T (CD3⁺ NKp46⁻) cells in spleen in isotype ($n=7$) vs. anti-PD-1 + anti-CTLA-4 (Dual ICI, $n=8$) NOD mice after 4 weeks. **b**, Relative frequency of activated T cells (CD44⁺ CD62L⁻) among CD4⁺ and CD8⁺ T cell subsets in spleen in isotype ($n=7$ or 8) and Dual ICI ($n=8$ or 10). **c**, Relative frequency of interferon (IFN)- γ ⁺ cells within CD4⁺ population between isotype ($n=7$) and Dual ICI-treated ($n=8$) mice. **d**, Relative frequency of IL-17A⁺ cells in CD4⁺ pop. between isotype ($n=14$) and Dual ICI-treated ($n=14$) mice. **e**, Representative histogram of ROR γ t⁺ by thyroid-infiltrating CD4⁺ cells from isotype vs. ICI-treated mice; 7 ICI treated and 8 isotype mice evaluated. **f**, Gating strategy for CD4⁺ and IL-17A⁺ populations from spleen, and relative frequency of CD4⁺ and CD4⁻ IL-17A⁺ cells in spleen from isotype ($n=12$) and Dual ICI-treated ($n=10$) mice. **g**, Frequency of IL-17A⁺ cells within gamma delta ($\gamma\delta$) cells in spleen from isotype ($n=12$) and Dual ICI-treated ($n=10$) mice. Data are mean. * $p<0.05$, two-tailed, unpaired t test with Welch correction, assuming unequal s.d., and Holm-Sidak method correction for multiple comparisons (**a-d,f,g**).

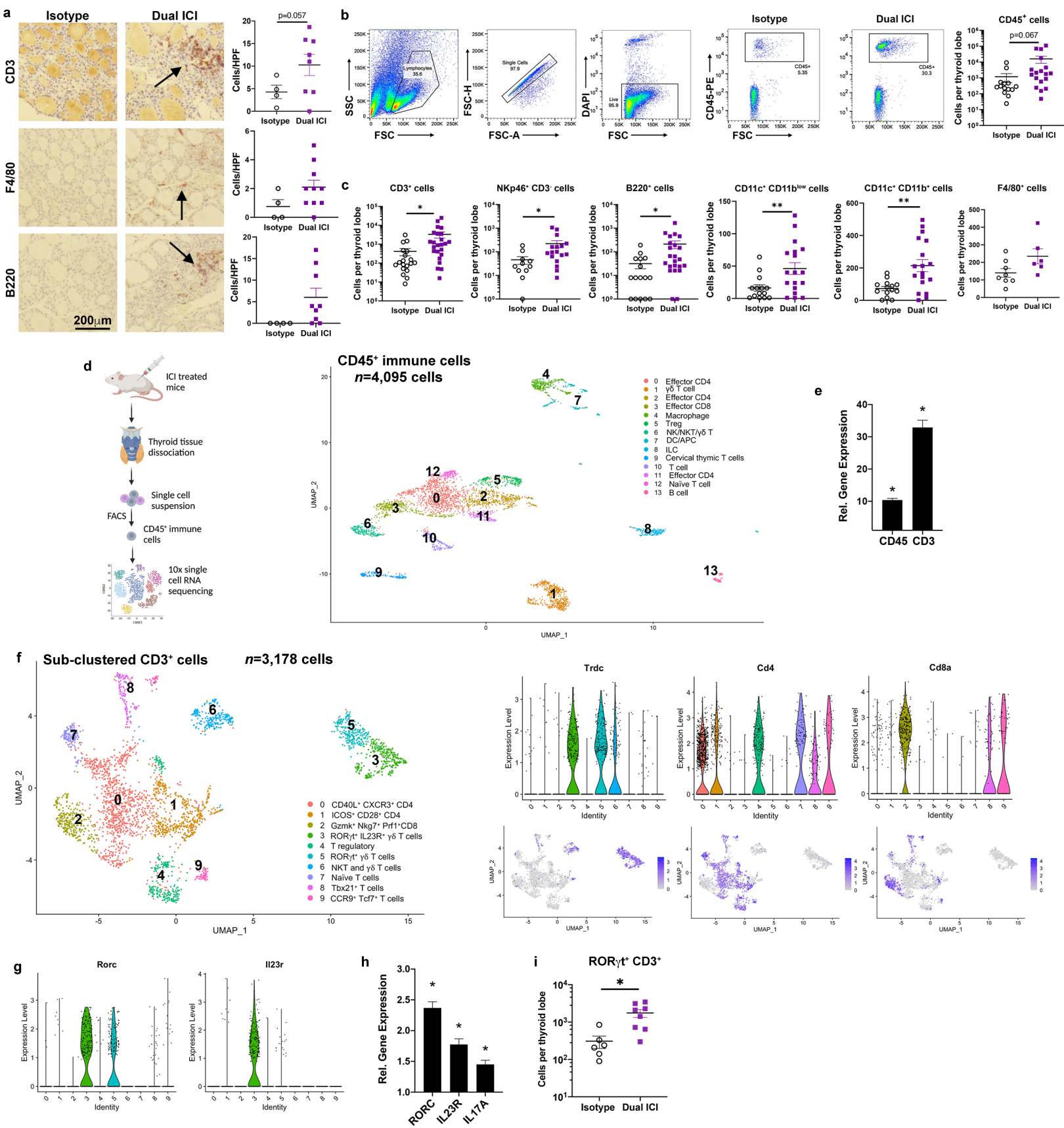


Figure 3. Characterization of thyroid-infiltrating immune cells in ICI-treated NOD mice.

a, IHC staining for T cells (CD3), macrophages (F4/80), and B cells (B220) in thyroid tissue from Dual ICI- ($n=7, 10, \text{ or } 9$) vs. isotype- ($n=4$) treated mice [*left*, representative sections, 400x original mag.; *right*, cells/hpf]. **b**, Representative gating strategies and dot plots (*left*) and relative frequency of CD45⁺ immune cells in thyroid tissue (*right*, cells per thyroid lobe) from isotype ($n=11$) vs. Dual ICI ($n=17$) treated mice after 4 weeks. **c**, Relative frequency of immune subpopulations in isotype ($n=11$, except $n=16$ for CD3⁺ and B220⁺) vs. Dual ICI-treated ($n=17$, except $n=23$ for CD3⁺ and B220⁺) mice. **d**, Schematic of tissue processing for single cell RNA sequencing (*left*). UMAP plot of 4,095 thyroid-infiltrating CD45⁺ immune cells from 10 pooled Dual ICI-treated mice, 2 independent experiments (*right*). Cluster analysis yields 14 distinct clusters comprising CD4, CD8, and $\gamma\delta$ T cells, natural killer (NK)/NKT cells, innate lymphoid cells (ILC), B cells, macrophages, and dendritic (DC)/antigen presenting cells (APC). **e**, Intrathyroidal gene expression for *Cd45* and *Cd3e* in ICI-treated vs. isotype mice measured by qRT-PCR. **f**, UMAP of CD3-subclustered cells, $n= 3,178$ cells. Cluster analysis yields 10 distinct clusters comprising CD4, CD8, and $\gamma\delta$ T cells (*left*). Feature and violin plots for T cell subset markers for $\delta\gamma$ (*Trdc*), CD4 (*Cd4*), and CD8 (*Cd8a*) (*right*). **g**, Violin plots for type 3 immunity (ROR γ t-pathway) associated genes *Rorc* and *Il23r*. **h**, Intrathyroidal gene expression for *Rorc*, *Il23r*, and *Il17a* in ICI-treated vs. isotype mice, by qRT-PCR. **i**, Comparison of thyroid-infiltrating ROR γ t⁺ pan-CD3⁺ ($\alpha\beta$ and $\gamma\delta$) T cells by flow cytometry in ICI-treated ($n=8$) vs. isotype ($n=6$) mice. Data are mean \pm SEM. For qRT-PCR, mean fold change \pm SEM, $n=12$ animals/group; thyroid tissue pooled and run in 3 experiments, in triplicate. * $p<0.05$, ** $p<0.01$, two-tailed, unpaired t test with Welch correction, assuming unequal s.d. (**a-c,i**) and Holm-Sidak method correction for multiple comparisons (**e,h**).

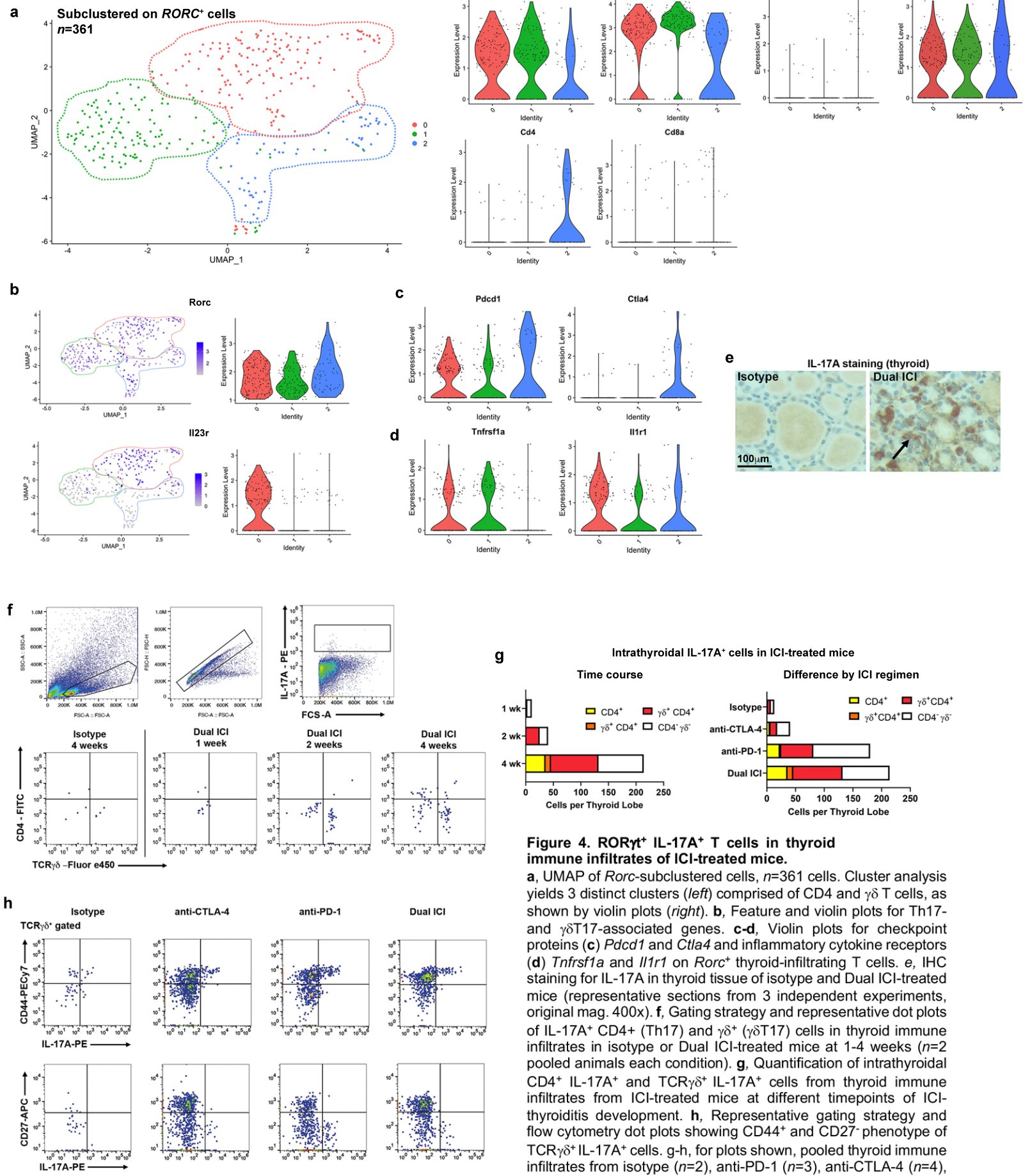


Figure 4. ROR γ t⁺ IL-17A⁺ T cells in thyroid immune infiltrates of ICI-treated mice.

a, UMAP of *Rorc*-subclustered cells, *n*=361 cells. Cluster analysis yields 3 distinct clusters (*left*) comprised of CD4⁺ and $\gamma\delta$ T cells, as shown by violin plots (*right*). **b**, Feature and violin plots for Th17- and $\gamma\delta$ T17-associated genes. **c-d**, Violin plots for checkpoint proteins (**c**) *Pdcd1* and *Ctla4* and inflammatory cytokine receptors (**d**) *Tnfrsf1a* and *Il1r1* on *Rorc*⁺ thyroid-infiltrating T cells. **e**, IHC staining for IL-17A in thyroid tissue of isotype and Dual ICI-treated mice (representative sections from 3 independent experiments, original mag. 400x). **f**, Gating strategy and representative dot plots of IL-17A⁺ CD4⁺ (Th17) and $\gamma\delta^+$ ($\gamma\delta$ T17) cells in thyroid immune infiltrates in isotype or Dual ICI-treated mice at 1-4 weeks (*n*=2 pooled animals each condition). **g**, Quantification of intrathyroidal CD4⁺ IL-17A⁺ and TCR $\gamma\delta^+$ IL-17A⁺ cells from thyroid immune infiltrates from ICI-treated mice at different timepoints of ICI-thyroiditis development. **h**, Representative gating strategy and flow cytometry dot plots showing CD44⁺ and CD27⁻ phenotype of TCR $\gamma\delta^+$ IL-17A⁺ cells. g-h, for plots shown, pooled thyroid immune infiltrates from isotype (*n*=2), anti-PD-1 (*n*=3), anti-CTLA-4 (*n*=4), and Dual ICI (*n*=2) treated mice after 4 weeks, or sooner timepoints (*n*=2) from Dual ICI treated for Time Course.

Lechner et al. Figure 6

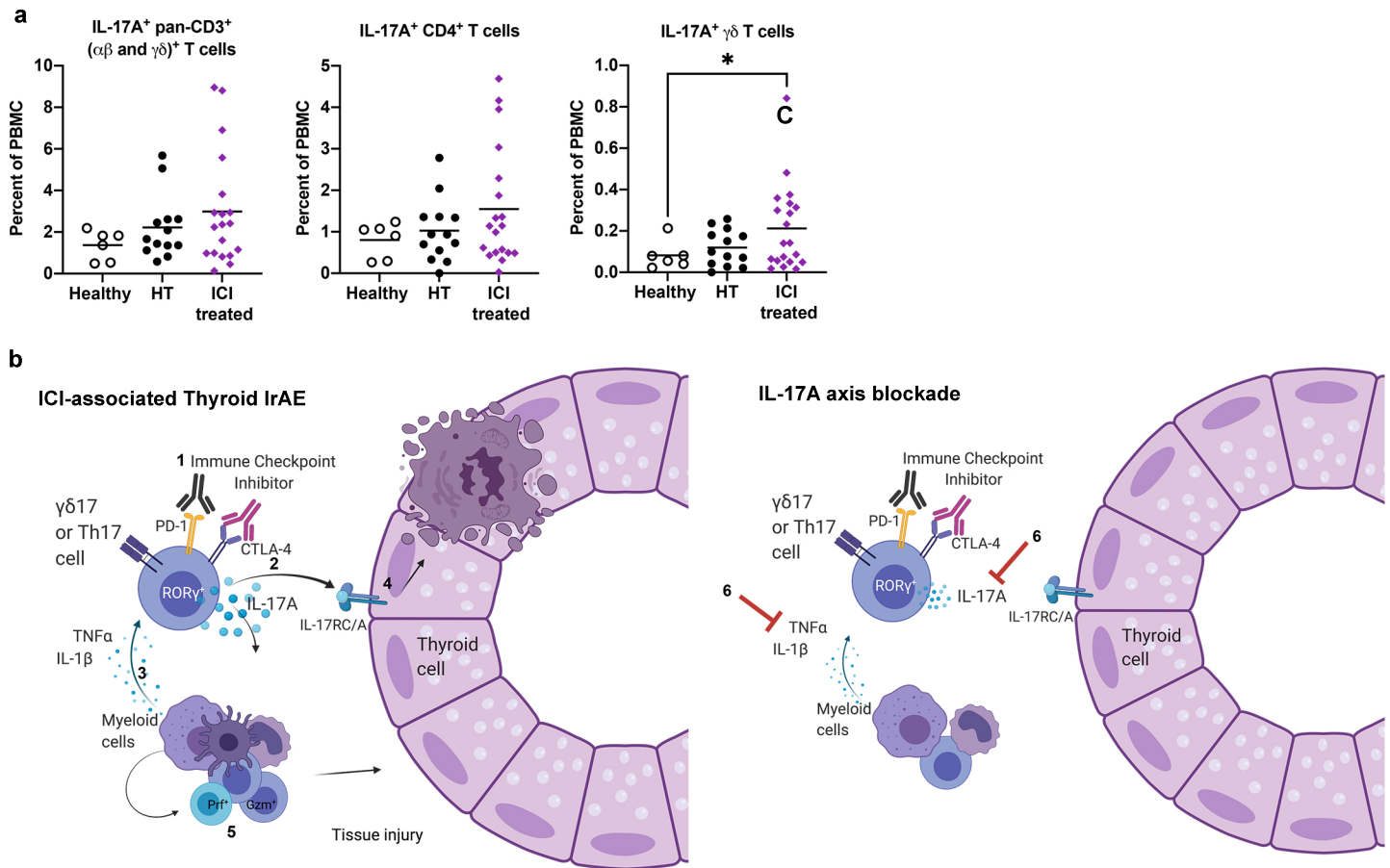


Figure 6. $\gamma\delta$ T17 and Th17 cells in ICI-treated cancer patients.

a, Relative frequency of IL-17A⁺ pan-CD3⁺, Th17, and $\gamma\delta$ T17 cells in peripheral blood of controls ($n=6$), patients with Hashimoto's thyroiditis (HT, $n=13$), or patients with cancer treated with ICI ($n=20$). Mean shown. * $p<0.05$. Brown-Forsythe ANOVA, assuming unequal s.d., followed by Dunnett's multiple comparisons test. **b**, Proposed mechanism of Thyroid IrAE. (1) ROR γ t⁺ Th17 and $\gamma\delta$ T17 cells may be activated by anti-PD-1 and/or anti-CTLA-4 inhibitor binding to (2) release IL-17A. (3) In addition, myeloid cells within the thyroid may contribute to Th17 and $\gamma\delta$ T17 activation and recruitment by production inflammatory cytokines IL-1 β and TNF α and chemokines. IL-17A within the thyroid microenvironment may affect thyroid follicular cell death via (4) induction of apoptosis or indirectly by (5) facilitating the accumulation of cytotoxic effector cells. (6) Strategies to reduce IrAE target the IL-17A axis.

Supplementary Files

This is a list of supplementary files associated with this preprint. Click to download.

- [SupplementalMethods.pdf](#)
- [Extendeddatafiles.pdf](#)
- [ExtDataTable1TopGeneExpressionscRNAseq.xls](#)
- [ExtDataTable2CellChat.xlsx](#)